Cloud height measurement by a network of all-sky-imagers

Niklas Benedikt Blum[1,2], Bijan Nouri[1], Stefan Wilbert[1], Thomas Schmidt[2], Ontje Lünsdorf[2], Jonas Stührenberg[2], Detlev Heinemann[2], Andreas Kazantzidis[3], and Robert Pitz-Paal[4]

[1]Deutsches Zentrum für Luft- und Raumfahrt (DLR), Institut für Solarforschung, Paseo de Almería, 73, 2, E-04001 Almeria, Spain
[2]Deutsches Zentrum für Luft- und Raumfahrt (DLR), Institut für Vernetzte Energiesysteme, Carl-von-Ossietzky-Straße 15, 26129 Oldenburg, Germany
[3]Laboratory of Atmospheric Physics, Department of Physics, University of Patras, 26500 Patras, Greece
[4]DLR, Institut für Solarforschung, Linder Höhe, 51147 Köln, Germany

Correspondence: Niklas Blum (niklas.blum@dlr.de)

Abstract. Cloud base height (CBH) is an important parameter for many applications such as aviation, climatology or solar irradiance nowcasting (forecasting for the next seconds to hours ahead). The latter application is of increasing importance to operate distribution grids as well as photovoltaic power plants, energy storage systems and flexible consumers.

To nowcast solar irradiance, systems based on all-sky-imagers (ASIs), cameras monitoring the entire sky dome above their point of installation, have been demonstrated. Accurate knowledge of CBH is required to nowcast the spatial distribution of solar irradiance around the ASI's location at a resolution down to $5\ \mathrm{m}$. Two ASIs located at a distance of usually less than $6\ \mathrm{km}$ can be combined into an ASI-pair to measure CBH. However, the accuracy of such systems is limited. We present and validate a method to measure CBH using a network of ASIs to enhance accuracy. To the best of our knowledge, this is the first method to measure CBH by a network of ASIs which is demonstrated experimentally.

In this study, the deviations of 42 ASI-pairs are studied in comparison to a ceilometer and characterized by camera distance. The ASI-pairs are formed from seven ASIs and feature camera distances of $0.8...5.7\ \mathrm{km}$. Each of the 21 ~~ASI-tuples~~ tuples of two ASIs formed from seven ASIs yields two independent ASI-pairs as the ASI used as main and auxiliary camera respectively is swapped. Deviations found are compiled into conditional probabilities telling how probable it is to receive a certain reading of CBH from an ASI-pair given that true CBH takes on some specific value. Based on such statistical knowledge, in the inference the likeliest actual CBH is estimated from the readings of all 42 ASI-pairs.

Based on the validation results, ASI-pairs with small camera distance (especially if $< 1.2\ \mathrm{km}$) are accurate for low clouds ($\mathrm{CBH} < 4\ \mathrm{km}$). In contrast, ASI-pairs with camera distance of more than $3\ \mathrm{km}$ provide smaller deviations for greater CBH. No ASI-pair provides most accurate measurements under all conditions. The presented network of ASIs at different distances proves that, under all cloud conditions, the measurements of CBH are more accurate than using a single ASI-pair.

1 Introduction

Cloud base height (CBH) has become an important parameter in meteorology that is required, either directly or indirectly, in many applications. CBH is used to validate and improve climate models (Costa-Surós et al., 2013) and numeric weather prediction models (Hogan et al., 2009). In aviation, CBH is important to air traffic controllers (Khlopenkov et al., 2019; Reynolds et al., 2012; Isaac et al., 2014). As clouds are the major cause of variability of the solar resource, they are of special interest for solar power applications. Here, CBH is of interest to forecast the solar resource for the next seconds to hours ahead (nowcasting). All-sky-imager (ASI)-based nowcast methods require cloud top height (CTH) and CBH to calculate the position and extent of cloud shadows on the ground (Nguyen and Kleissl, 2014). In a similar way, satellite-based nowcast methods can profit from accurate knowledge of CBH and CTH (Bieliński, 2020). The statistical relationship between CBH and a cloud's further properties like optical thickness can be exploited to support the generation of such nowcasts (Nouri et al., 2019c). Also, cloud tracking schemes, used in ASI-based nowcasting, require knowledge of CBH to estimate the absolute displacement of clouds over time.

The method to measure CBH, presented in this study, is used as part of an ASI-based nowcasting system of the solar resource. ASI-based nowcasting is typically applied if variations of irradiance have to be predicted for lead times immediately ahead (0…20 min) and at highest temporal and spatial resolution (e.g. 30 s and 5 m respectively as used by Nouri et al., 2020b). Such nowcasts can reduce the uncertainty of supply from solar power plants and can support efficient balancing of energy supply and demand (Law et al., 2014; Kaur et al., 2016). Further, they can be applied to control concentrating solar power plants (Nouri et al., 2020a) more efficiently. The coordination of renewable production and energy consumption at a local scale is a way to minimize requirements on grid-infrastructure while keeping curtailment of feed-ins from renewable sources at a low level. Ghosh et al. (2016) use nowcasts (15 s ahead) to control PV-feed in and provide reactive power. In this context, spatially and temporally highly resolved nowcasts enable distribution grid operators, microgrid controllers and energy management administrators to control backup power, energy storage and flexible consumers. Cirés et al. (2019) pointed out the potential of nowcasts to reduce battery storage capacities required by PV plants under ramp rate restrictions. As implied above, high quality and real time information of local CBH is required at all sites for which accurate nowcasts should be provided.

CBH~~is commonly~~, required in ASI-based nowcasting, can be estimated in multiple ways. Most commonly, CBH is measured by ceilometers or other LiDARs. In Germany, the meteorological service Deutscher Wetterdienst (DWD) operates a network of ceilometers which has a distance between stations of approximately 60 km in the region of the measurement site Oldenburg (Chan et al., 2018). Ceilometers are specialized instruments that come at a high price and provide CBH zenith-wise for the location of their installation. Therefore, we do not consider ceilometers as an option to provide CBH in real time for most solar power plants or cities with many roof top installations. Further ~~,~~common approaches to measure CBH, which could be applied for operational use in nowcasting~~. Among others, these ,~~ include weather balloons and the estimation of CBH based on a recognized cloud genus (World Meteorological Organization, 2018). Satellites can measure CTH of the highest cloud layer (Hamann et al., 2014) but require estimations of cloud vertical extent (see e.g. Noh et al., 2017) to provide cloud base height (CBH). ASIs can directly measure CBH but require estimations of cloud vertical extent if CTH is of interest. ~~This approach is~~

~~especially reasonable if ASIs are used at a site for further purposes such as~~ In ASI-based nowcasting, the double use of ASIs for the estimation of CBH besides cloud recognition is considered advantageous in a trade-off between system costs and accuracy. ~~ASI-based nowcasting is typically applied if variations of irradiance have to be predicted for lead times immediately ahead (0…20 min) and at highest temporal and spatial resolution (e.g. 30 s and 5 m respectively as used by Nouri et al., 2020b).~~

ASI-based estimation of CBH may follow different principles. Some approaches first measure the angular velocity of clouds in the sky-image of a single ASI and estimate CBH with an external source of cloud velocity. Wang et al. (2016) derives cloud velocity by three photocells placed at known distances from each other. Kuhn et al. (2018b) measures cloud velocity by a cloud speed sensor based on nine photocells and by a shadow camera system and compares the accuracy of received CBH. Tomographic reconstruction approaches (Mejia et al., 2018) or similarly voxel carving approaches (Nouri et al., 2018) first model 3-dimensional representations of clouds from which their base height can be retrieved.

Stereoscopic approaches match features found in the images of two ASIs. Used ASIs are located in proximity to each other, this way forming an ASI-pair. From the position of matched features in both images, CBH is triangulated. The literature describes various image features which can be utilized for this task. Blanc et al. (2017) exploits gradients of intensity. Allmen and Kegelmeyer Jr (1996) used local velocity in an image point derived by optical flow. Similarly, Savoy et al. (2016) utilized three-dimensional scene-flow making use of the slow evolution of cloud structures. Kuhn et al. (2018b) subtract red-channel images taken with a temporal offset of 30 s and match image areas with the most significant changes. Features from the images of both cameras are typically matched by block-wise cross-correlation while the used block size may vary between the approaches. Beekmans et al. (2016) generated dense 3-D representations of cumulus clouds using semi-global block-matching with a very fine block size of 11×11 pixels. Image areas, for which features are retrieved, are often restricted to areas that are segmented as cloud in a prior step (e.g. Blanc et al., 2017; Peng et al., 2015). The stereoscopic approach utilized here (Nouri et al., 2019a) enhances the approach by Kuhn et al. (2018b) and works completely independently from cloud recognition which is considered to bring a greater robustness. While stereoscopic and voxel carving/ tomographic approaches are in principle competing techniques, Nouri et al. (2019a) demonstrated, that voxel carving-based cloud modelling can be enhanced by incorporating CBH from a stereoscopic procedure.

Most ~~ASI-systems~~ ASI-based nowcasting systems described in the literature feature one (Schmidt et al., 2016), two (Allmen and Kegelmeyer Jr, 1996; Beekmans et al., 2016; Blanc et al., 2017; Savoy et al., 2016) or three (Peng et al., 2015) ASIs. Four ASIs have been used by (Kuhn et al., 2018a; Nouri et al., 2019a) and such systems are available at four different sites (Nouri et al., 2020b). A network of six ASIs accompanied the HOPE measurement-campaign in 2013 around Jülich, Germany (Macke et al., 2017). In the city state of Singapore, a larger number of 16 ASIs, interacting in a network to monitor the sky and clouds (in the following referred to as ASI network), has been set up (Sky cameras, 2020). A method to monitor clouds with an ASI network using tomographic reconstruction has been described conceptually and based on synthetic data by Mejia et al. (2018). Aides et al. (2020) studied a similar approach experimentally using an actual ASI network of up to 14 cameras located in an area of $12\ \mathrm{km} \times 12\ \mathrm{km}$ around Haifa, Israel. ASI-networks have additionally been reported in astronomy, to track meteorites during nighttime (Howie et al., 2017).

In this study, seven of the ASIs included in the Eye2Sky ASI network (Schmidt et al., 2019; Blum et al., 2019a, b) are used. The selected ASIs are located in the city of Oldenburg. At the moment of writing, Eye2Sky contains 24 ASIs in Oldenburg and a region of about $110\ \mathrm{km} \times 100\ \mathrm{km}$ to the west of Oldenburg. ~~An approach is presented to measure CBHby the ASI network that allows the use of~~ Eye2Sky is mainly dedicated to nowcasting of solar irradiance at high spatial and temporal resolution. The forecasting procedure, which will be described in more detail in a future publication, first recognizes clouds from the images of the ASIs. Cloud observations are then projected into a horizontal plane at the current CBH. These georeferenced cloud observations of multiple ASIs are merged and cloud properties are estimated. The angular velocities of clouds, as recognized by the individual ASIs, are transformed into absolute velocities over ground relying on an accurate estimation of CBH. Clouds are tracked along received cloud motion vectors to predict the clouds' future positions. Prior works studying ASI-based forecasting systems with up to four cameras (e.g. Nouri et al., 2019b) suggested that CBH is an essential component when predicting maps of solar irradiance based on cloud observations from ASIs, as the current and future positions of cloud shadows on the ground can only be predicted accurately if the clouds' height and velocity are determined accurately. Thus, in this publication an important component of this nowcasting system, namely the estimation of CBH, is presented. Our approach allows to use multiple ASI-pairs ~~in proximity simultaneously~~organized as ASI network and located in proximity, to estimate CBH. 42 ASI-pairs are formed from the seven ASIs and CBH is estimated by each ASI-pair based on the method presented by Nouri et al. (2019a). In a period of three months, the accuracy of the included ASI-pairs is evaluated for distinct conditions. Gained knowledge about the deviations of each ASI-pair is applied to merge the measurements of CBH from all 42 ASI-pairs into a more reliable measurement.

This publication is structured as follows. First, Eye2Sky, the ASI network used in the experiments, is introduced (Sect. 2). Then, the measurement procedure of CBH using the ASI network is presented (Sect. 3). Here, the properties of CBH measured by reference ceilometer and by 42 ASI-pairs are discussed (Sect. 3.1). The meteorological conditions at the site are studied next (Sect. 3.2). In Sect. 3.4 and Sect. 3.3, a novel procedure to combine CBH measurements from multiple ASI-pairs of the ASI network is presented. Section 4 analyzes CBH measurement by the ASI network in comparison to the individual ASI-pairs for all relevant conditions. A summary of the presented findings closes the study in Sect. 5.

2 Eye2Sky network and experimental setup

The so called Eye2Sky ASI network is being set up in the region of Oldenburg (Fig. 1, left). At its full extent, Eye2Sky will include 38 stations distributed over an area of roughly $110\ \mathrm{km} \times 100\ \mathrm{km}$ equipped with ASIs. 13 of these stations will be supported by additional meteorological measurements to provide beam, diffuse and global irradiance via rotating shadowband irradiometers as well as ambient temperature and relative humidity. Eight ceilometers will be included in the network. Six of these are operated by the meteorological service Deutscher Wetterdienst (DWD). Five of these ceilometers are in the region viewed in Fig. 1. Several PV plants and numerous smaller distributed PV installations are also present in the study area. With its regional coverage, Eye2Sky aims to achieve nowcasts for individual PV installations from some minutes to multiple hours ahead. In the urban area of Oldenburg, the network will feature a high density of 14 ASIs in an area of $13\ \mathrm{km} \times 12\ \mathrm{km}$. This

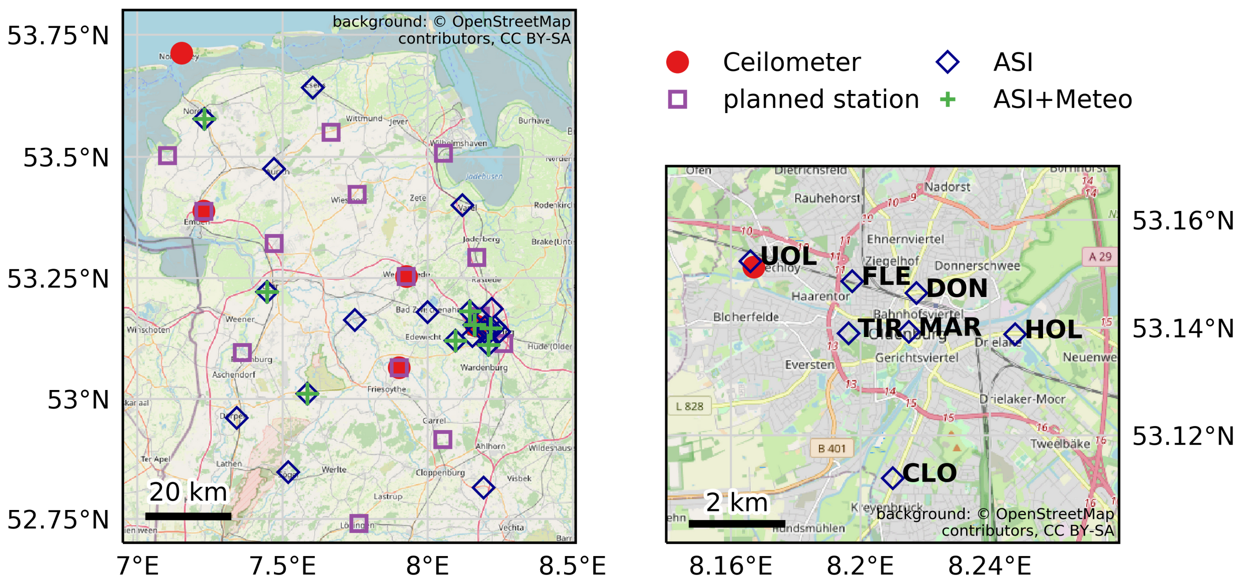

Figure 1. Overview of the Eye2Sky ASI network including operational ASIs (ASI), radiometric measurements (Meteo) as well as planned stations (left) and ASIs in the city of Oldenburg included in this study (right). The ceilometer used as reference (marked by a red circle in the right figure) is located near the northwest-most ASI UOL. (background: © OpenStreetMap contributors 2020. Distributed under a Creative Commons BY-SA License.)

dense setup aims to provide ASI-based nowcasts of high accuracy across the urban area and reliable estimation of CBH under all conditions is an important contribution to achieve this scope.

This work utilizes seven ASIs and one ceilometer located in the city of Oldenburg (Fig. 1, right). The ceilometer is located $133\ \mathrm{m}$ southeast of to the most northwestern ASI UOL. All included ASIs except for UOL are located east and south of the ceilometer. ASIs are placed at most $5.7\ \mathrm{km}$ from this ceilometer.

For this study, these ASIs are arranged into several ASI-pairs as defined by ~~arbitrarily~~ iteratively selecting a tuple of ~~ASIs (~~two ASIs out of the 21 tuples ~~are available)~~ available and forming two independent ASI-pairs from each tuple by swapping its main camera. The main camera of an ASI-pair is central to the measurement of CBH through an ASI-pair, described in more detail in Sect. ~~3.1~~3.1, and defines the center of the area for which CBH is estimated. From 21 ~~ASI-tuples~~tuples of 2 ASIs, 42 ASI-pairs are received. All 42 ASI-pairs are included in the estimation procedure. The paired cameras' distance and the orientation of the ~~camera~~ ASI-pair's axis characterize the ASI-pairs. The orientation of ~~a camera~~ an ASI-pair's axis is defined as seen from the main ASI and given in degree north. Figure 2 shows the distribution of orientations of ~~camera~~ ASI-pair's axes (left) and camera distances (right) in the set of available ASI-pairs. This set covers almost all possible orientations of ~~camera~~

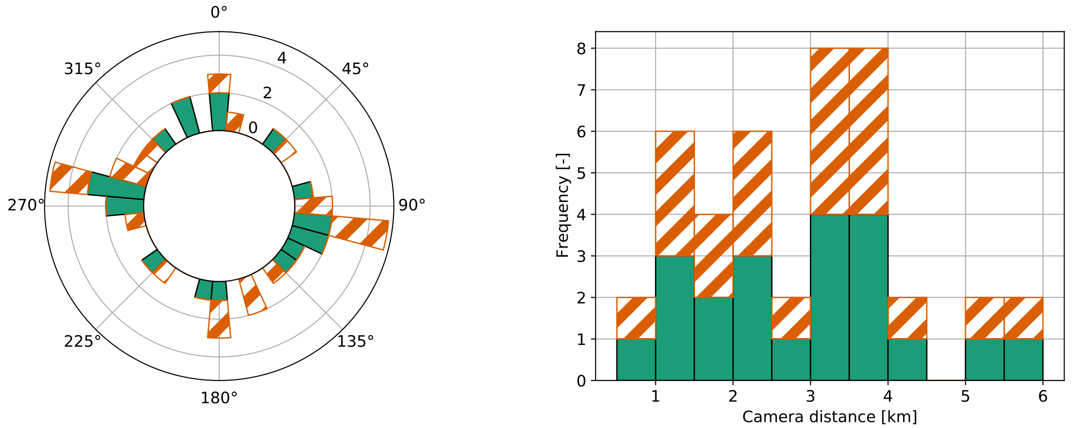

Figure 2. Frequency distribution of ~~camera axis~~ the bearing angles of the ASI-pairs' axes in the set of available ASI-pairs (over north, left) and of available camera distances (right) resulting when arranging the seven ASIs in the urban area into 42 ASI-pairs (from each ~~ASI-tuple~~ 2-ASI-tuple two different ASI-pairs result by switching the main camera, counts of ASI-pairs with switched main camera are marked orange, striped)

ASI-pair's axes. Available camera distances $0.8 ... 5.7$ km cover most of the range $0.02 ... 5.5$ km that is used in literature (Kuhn et al., 2019). Only towards small camera distances below 0.8 km, the present set lacks further ASI-pairs.

The used ceilometer ~~is~~ of type Lufft CHM 15 k Nimbus ~~.~~ (firmware v0.747) is operated by DLR since 2018. CBH is measured by the manufacturer's *Sky Condition Algorithm* (Lufft, 2018) in the default configuration. Heese et al. (2010) specifies for a ceilometer of the same type, that full overlap of the laser's and the receiver's field of view is reached at a height of 1500 m. However relying on an overlap correction, the manufacturer specifies a minimum CBH of down to 0 m. In this study the manufacturer's default minimum CBH of 45 m is used.

The used ASIs are surveillance cameras of type Mobotix Q25 6MP color version (Mobotix, 2017) with a fisheye lens providing $180°$ field of view. The ASIs are configured to use a constant exposure time of 149 µs and a constant color temperature of 5500 K. The effective image resolution is 2048 pixel $\times$ 2112 pixel. An exemplary sky image from ASI UOL is shown in Fig. 3, left. The ASIs' intrinsic calibration was determined according to Scaramuzza et al. (2006). The ASIs' locations defined by latitude, longitude and altitude were identified in geolocated satellite images. Altitude was estimated based on the local altitude of the ground and the stations' height over ground. The exact orientation of the ASIs' field of view was computed from the trajectory of the full moon registered in nighttime images as described by Nouri et al. (2019a).

The ASIs provide sky images at every half and full minute. The ceilometer provides readings $0,\ 15,\ 30,\ 45$ s after each full minute. The clock of each measurement instrument is at any time synchronized via NTP (Network Time Protocol). Sky images, measurements of CBH and meteorological parameters are uploaded over the cellular network to a central server typically within 2.5 s and in most cases within 5 s after acquisition. A high-performance computer (HPC) is used to compute CBH from sky images. Image processing takes up the major share of the computation time required by the presented method. These tasks are performed in parallel for each of the seven ASIs (typically allocating 4 CPUs of 3.4 GHz and 1 GB memory to each ASI) avoiding redundant calculations. In this way, computational cost scales mostly linear with the number of ASIs used instead of with the number of ASI combinations so that execution in real time is possible. In total, including computation time, the estimation of CBH by the ASI network can be retrieved within 10 s after image acquisition. CBH is computed by the ASI-pairs and by the ASI network during daytime, i.e. if the sun elevation at the time of image acquisition is greater than 0°.

The dataset used in this study covers the period from 01 April 2019 through 27 September 2019. It is split into a period used for deriving the method (until 29 June 2019) and a period used for validations (starting from 30 June 2019). Time stamps from the validation period 30 June 2019 to 27 September 2019 are excluded from the model development and also from the estimation of conditional probabilities.

3 Development of a CBH estimation using the ASI network

In this section we present a procedure to estimate CBH by an ASI network. The procedure aims to be more accurate compared to an estimation of CBH by independent ASI-pairs. First, properties of the reference CBH received from a ceilometer and properties of CBH received from ASI-pairs are discussed. Next, meteorological conditions at the site are discussed which are relevant to the performance of a CBH measurement. Based on this, we develop the estimation which borrows principles from Maximum Likelihood Estimation (MLE).

3.1 Properties of CBH measurements from ceilometers and from ASI-pairs

As introduced in Sect. 2, a ceilometer of type Lufft CHM 15 k Nimbus is used as reference in the development and validation presented in this study. When low and optically thick clouds are present, only the lowest cloud layer is expected to be recognized reliably by the ceilometer~~and readings provided for .~~. Therefore, in the case of overlaid cloud layers~~are not evaluated.~~ , we only evaluate readings provided for the lowest layer. This approach applies to all evaluations presented in this publication.

Regarding the accuracy of ~~the instrument, a benchmark by Martucci et al. (2010) exhibited a bias~~ ceilometers in general, de Haij et al. (2016) and Görsdorf et al. (2016) noted that there is no generally excepted, quantifiable definition of CBH, yet. Further, due to a lack of reference measurements, benchmarks may typically focus on the consistency of CBH measurements by different types of ceilometers. In a benchmark performed by Martucci et al. (2010), the measurement of a Vaisala CL31 ceilometer CBH_{CL} showed a significant deviation from the reading CBH_{CHM} of the instrument ~~compared to another manufacturer's ceilometer of 160 m. With this in mind, we still consider the instrument to be sufficiently accurate for the scope of this study.~~ used here. This trend was given by $\mathrm{CBH}_{CL} = 160.315\ \mathrm{m} + 0.925 * \mathrm{CBH}_{CHM}$. However, the measurement procedure, of the instrument used here, was modified by firmware updates in the meantime. Görsdorf et al. (2016) presented results from a more recent measurement campaign, CeiLinEx2015, which took place in 2015. In this experiment the measurements of six types of ceilometers were compared. For stratus and stratocumulus clouds as well as for fog, deviations between the instruments of up to 70 m were observed. For each of these conditions, the CHM 15 k, used here, provided the smallest measurements of CBH

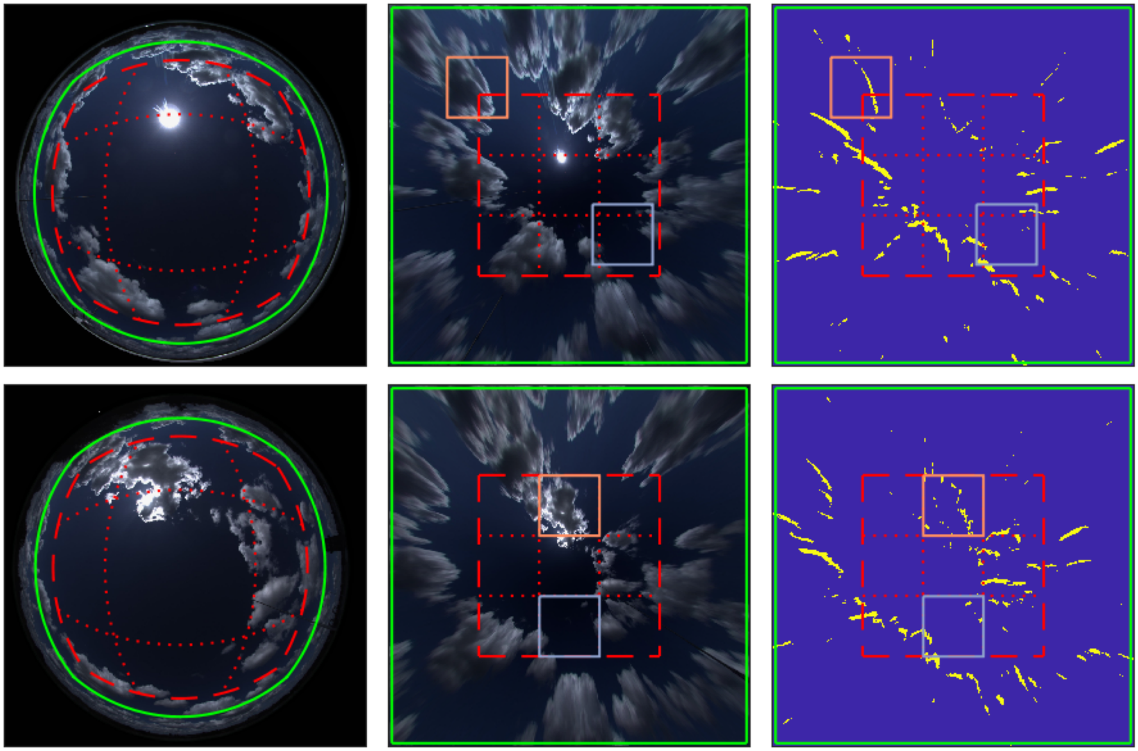

Figure 3. Sky ~~area (exemplary at UOL)~~ areas evaluated in the measurement of CBH exemplary for ASI-pair FLE-UOL, with ASI UOL in the top row and FLE in the bottom row. Maximum extent (solid green shape) and area used by the main camera in the default case (red dashed shape) in the distorted ASI image (left), in the undistorted ortho-image (center), in the binary red-channel difference image of two consecutive exposures (right). The binary red-channel difference image (right) shows areas considered as features in the cross-correlation for the comparison to the second camera as yellow shapes. A rejected match between the ASI images is marked orange, a valid match is marked light blue.

in terms of mean deviation from the median of all tested instruments. More severe deviations of several kilometers between the instrument types were observed during conditions with heavy rain.

In an acceptance test, de Haij et al. (2016) measured CBH by two CHM 15 k, by a Vaisala LD40 ceilometer, by a UV lidar (Leosphere ALS450) and by visibility sensors mounted in various altitudes on a tower of 213 m height. For CBH of up to 200 m, the CHM 15 k typically measured a CBH 30 . . . 50 m smaller than the one of the LD40. However, the CHM 15 k was in better agreement with the estimate based on visibility sensors. Görsdorf et al. (2016) and de Haij et al. (2016) suggest, that the negative mean deviation of the CHM 15 k attested by all these studies, for clouds in the range CBH < 3 km, is mostly caused by the manufacturers' algorithms to detect CBH from backscatter profiles. Whereas, according to the manufacturer (Lufft, 2018), the CHM 15 k detects the rising edge of a backscatter peak that exceeds a threshold, other manufacturers' devices may rather recognize the peak's maximum.

For the range of CBH in $3\ldots12$ km, an inspection of timeseries depicted by de Haij et al. (2016) indicates very good agreement of the measurements from CHM 15 k and the UV lidar, used there. As a further test of de Haij et al. (2016), performed at a resolution of 60 s, high clouds, detected by the UV lidar in a range of $6\ldots7.5$ km, were to be detected by the CHM 15 k within a tolerance of ±3 classes in hh code (WMO Table 1677). This tolerance corresponds to a CBH-range of ±1050 m centered around the discretized reference CBH. CHM 15 k was attested a probability of detection of $>98\%$ and a false alarm rate of 0%. Based on these studies, the accuracy of the reference instrument is expected to be adequate for the range of CBH <3 km and also for the range of CBH ≥3 km, a rather good performance of the instrument is indicated. The experimental results of this study will in particular be compared to prior studies which used a ceilometer of the same type. This is expected to avoid possible inconsistencies related to the used reference.

From all ASIs available in the urban area, we form independent ASI-pairs that measure CBH by a stereoscopic triangulation ~~method. The method used here~~ which was introduced by Kuhn et al. (2018b) and further refined by Nouri et al. (2019a). The algorithm used here to estimate CBH by the individual ASI-pairs has been described and validated in the latter publication. Nouri et al. (2019a) evaluated an ASI-pair with a camera distance of 495 m. For four ranges of reference CBH, defined by the bin edges 0, 3, 6, 9, 12 km, RMSDs of 0.6, 1.4, 3.2, 3.1 km were found for 10 min average CBH. The study did not provide information on BIAS. Further, in that validation, higher clouds were more frequent and no observations at a reference CBH of less than 1 km occured. The studies of Kuhn et al. (2018b) and Nouri et al. (2019a) were performed in Almería, Spain. Both studies validated the ASI-based measurement of CBH using a ceilometer of type Lufft CHM 15 k as reference. At this point we recapitulate aspects of the procedure which are important for the remaining publication. For a more detailed description, we refer to Nouri et al. (2019a).

Images from both ~~cameras~~ ASIs (e.g. UOL and FLE, see Fig. 3, left) are first projected into horizontal planes yielding orthogonal images (Fig. 3, center) by a well established method described e.g. by Luhmann (2000). Then, the difference in the red-channel ~~of consecutive images~~ compared to the image recorded 30 s before is calculated for ~~each camera~~the image of each ASI. Areas in the difference images of the two cameras, in which the red-channel changes most significantly (98-percentile) within the 30 s between consecutive images, are used as features (illustrated in Fig. 3, right) to be matched by block-wise correlation. With the known camera distance, a shift received in cross-correlation is translated into a height of the feature over ground.

In practice, the triangulation relies on cloud edges which are visible from both perspectives and provide sufficient contrast. Therefore, the method responds stronger to optically dense clouds, especially in the proximity of the sun~~(Kuhn et al., 2018b)~~, as found by Kuhn et al. (2018b). Moreover, we do not exactly measure CBH but the height of these distinct cloud edges. We expect to introduce a small bias when using this cloud height as CBH. Nouri et al. (2019a) analyzed sources of deviations when estimating CBH by an ASI-pair. In accordance with that study, we expect this bias to be acceptable compared to other uncertainties and to be in the order of 100 m.

In ~~the present study~~accordance with the system used by Nouri et al. (2019a), we use a cascading procedure to estimate CBH robustly also in conditions with low sky coverage. ~~We first project the field of view of each camera up to a~~ First, the main ASI's orthogonal image is restricted to a square-shaped area (Fig. 3, red dashed shape) defined by a maximum zenith angle of 67°, measured ~~at~~ in the center of each ~~image side , into an orthoimage of square shape~~ side of the square. In a cross-correlation, each of the nine squares confined by dotted or dashed lines (also known as windows, Fig. 3, bottom, right) from the orthoimage of the main ASI is matched with an area of identical shape from the orthoimage of the second ASI (Fig. 3, ~~red dashed shape). In the correlation, the central area (or window,~~ top, right). With the known camera distance, the shift is converted into a measurement of CBH.

If the estimation of CBH failed for one of the windows, valid readings from neighboring ones are averaged ignoring any window for which the estimation failed. In cases with no valid measurement in any of the windows, the orthogonal images of both ASIs are evaluated up to a maximum zenith angle of 77.8° (measured at the center of each image side, green shapes in Fig. 3~~, central red dotted box)from~~). These orthoimages from both cameras are matched in the cross-correlation and the ASI-pair returns a uniform CBH. This second step can yield a valid measurement of CBH in cases when only few clouds are present to be matched. This step mainly intends to increase the robustness of the CBH measurement. This step is not expected to increase the capability of an ASI-pair to detect very low clouds in relation to the camera distance, as the window size used in this step is very large.

As a modification of the ~~orthoimage of the main camera is matched with a window of identical dimensions from the~~ method by Nouri et al. (2019a), we only use CBH provided for the central point of the orthoimage of the ~~second camera. This central~~ main ASI, corresponding to a zenith angle of 0°. This procedure is followed for both the ASI-pairs and for the ASI network using these ASI-pairs. We expect that ASI-based measurement of CBH is most accurate for this central point. This point receives CBH primarily from matches involving the central window of the ~~orthoimage~~ main ASI's orthoimage, which is less affected by image distortion. The central window of the main ~~camera~~ ASI's orthoimage covers zenith angles up to 38.1°, measured at the center of each window side. ~~Therefore~~Thus, a CBH measurement for a square-shaped area around the main ~~camera~~ASI's location is yielded. For example, the area's side lengths measure 1.6, 4.7, 7.8, 15.7 km for a respective CBH of 1, 3, 5, 10 km.

~~If the estimation of CBH fails for~~ Only based on geometry and the evaluated image areas, this central window ~~, we use the CBH that is measured by matching the peripheral windows (Fig. 3, peripheral red dotted boxes) of the same orthoimage with the orthoimage of the second camera. These peripheral windowsof an orthoimage have the same shape as the central window (see~~ could provide readings down to a minimum CBH of $0.25 \times d$. Where d is the camera distance. However, under such extreme conditions the matching procedure may fail very frequently. The central peripheral windows, shown in Fig. 3, ~~center, peripheral red dotted boxes). If a valid estimation of CBH is received for multiple peripheral windows, we use the average CBHfrom these windows.~~

~~For cases with still no valid measurement, images of both cameras are evaluated up to a maximum zenith angle of~~ approximately cover zenith angles 38.1..67°. The matched area from the auxiliary ASI's orthogonal image has identical shape and can cover a zenith angle up to 77.8° ~~(measured at~~. Based on this, we estimate the minimum CBH, which an ASI-pair can measure, to be $0.18 \times d$. However, from our experience, a large fraction of clouds observed at zenith angles larger than 67° are not matched successfully between the ASIs and typically rejected. If the matching procedure could only be successful, if also the window of

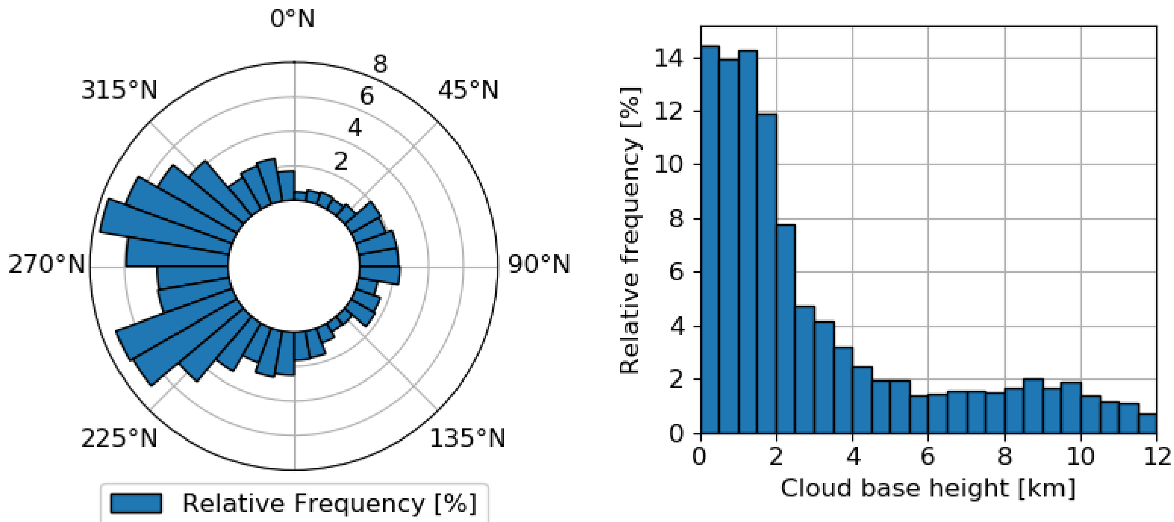

Figure 4. Wind rose of cloud motion directions derived from UOL camera indicating a dominance of clouds coming from western directions (left) and distribution of cloud base height (CBH) in the analyzed period (right)

the second ASI included zenith angles not larger than 67°, then CBH could be measured down to $0.32 \times d$ using the peripheral windows and $0.64 \times d$ using the central window.

This central point of the orthoimage, used here, was also in the ~~center of each image side). These image areas are projected into orthoimages (green shapes in Fig. 3). Resulting orthoimages from both cameras are matched in the cross-correlation~~focus of the validation presented by Nouri et al. (2019a) as the ceilometer was placed at one ASI's location and as observed CBH values were not smaller than 1 km. Overall, we expect that, by applying cross-correlation to binary difference images, our measurement approximates the median CBH of the cloud layer that is locally most dominant in ~~the sense of~~ features, driven by area and optical thickness.

A previous study by Kuhn et al. (2019) showed that camera distance and CBH itself significantly influence the accuracy received in the measurement of CBH by an ASI-pair with the present approach. Based on this, we use camera distance and CBH to characterize ASI-pairs.

3.2 Meteorological conditions at the site

To understand the performance of the CBH measurement based on ASI-pairs we briefly analyze the meteorological conditions on-site based on ceilometer and ASI data. Using ASI UOL we study the dominant directions of cloud motion at the site. Nouri et al. (2019a) found a root mean squared deviation (RMSD) of 17° for the estimation of the direction of cloud motion based on an ASI-pair. Based on this, we consider the estimation of cloud motion directions from ASI UOL as sufficiently accurate for this statistical evaluation. Figure 4 left shows the distribution of cloud motion directions estimated with the ASI in the sense of a wind rose representing the directions from which clouds approach the urban area. Two main lobes at azimuthal angles of 240°N (west to south-west) and 290°N (west to north-west) are seen while other directions of cloud motion are observed rather seldom.

The distribution of CBH at the site of Oldenburg for the full measuring period is given in Fig. 4 right. As in general in this study, the analysis is based only on the lowest cloud layer detected by the ceilometer. The majority of all ceilometer readings (54 %) indicates a CBH smaller than 2 km. Within the interval CBH $\in]0,2[$ km all values are observed similarly frequent. This includes the lowest bin of CBH $\in]0,0.5[$ km which indicates conditions with fog or low stratus clouds. For the majority of situations, it is of special interest to receive accurate measurements in the low range of CBH. Moreover, 28% and 18% of readings are found respectively in the intermediate range of CBH $\in [2,6[$ km and in the range of large CBH $\in [6,12[$ km. Within the range of high clouds, a roll-off of the frequency is seen for CBH > 10 km. A reliable estimation of CBH should therefore provide accurate readings for the range of CBH $\in]0,12[$ km.

A visual analysis and a k-means classification for the site of Oldenburg (not shown) suggested that local conditions predominantly feature distinct cloud layers with temporally low vertical variability. The major cause of variable CBH is found in the transitions between cloud layers. It is concluded that for sites with similar meteorological conditions, it is most important to measure CBH of the cloud layer which is most dominant at the evaluated time as accurately as possible. Kottek et al. (2006) characterize the climate in Oldenburg as warm temperate, fully humid with warm summers (Cfb). In this publication a summer half-year period (April...September) is studied. The climate is strongly influenced by the North Sea which is located at a distance of roughly 70 km. Eye2Sky and especially Oldenburg are situated in a plane with a maximum elevation over sea level of less than 160 m including vegetation and human infrastructure~~(TanDEM-X topographic data used in this study is described by Wessel et al~~ , as we calculated from the TanDEM-X elevation model (Wessel et al., 2018). The flat topography is expected to support a temporally and spatially low variability of CBH within cloud layers. For other sites, a focus on measuring CBH for every cloud object is of higher priority. For example, Tabernas, the site studied by Nouri et al. (2019a), features a cold-arid steppe climate (BSk according to Kottek et al., 2006) and is surrounded by mountains with elevations up to 2168 m over sea level within a radius of 25 km. As shown by (Nouri et al., 2019c), CBH at the site is distributed almost uniform in the range 0...11 km. These characteristics are expected to cause greater temporal and spatial variability of CBH. To conclude, a procedure, which estimates CBH of the cloud layer most dominant in the urban area of Oldenburg accurately, is considered beneficial to assess and model clouds in the same area (depicted in Fig. 1, right). Still, if clouds over the whole region covered by Eye2Sky (depicted in Fig. 1, left) are assessed, this method alone may not be sufficient. In the future, local cloud conditions may be classified by image processing techniques (e.g. Fabel et al., 2021) and CBH may be assigned to local clouds from clouds of the same type, which were recently observed in the urban area.

3.3 Estimating CBH in the ASI network (ORDER OF SECTIONS 3.3 AND 3.4 WAS EXCHANGED)

~~The estimation procedure presented here is motivated by~~ In this section we present our method to combine the measurements of CBH from a large number ASI-pairs organized as network. Prior works estimated CBH by a small number of two or in some cases four ASIs (Nouri et al., 2019a). However, with a large number of ASI-pairs, we consider a statistical method promising, which analyzes the CBH samples received and, based on the known characteristics of each ASI-pair, determines

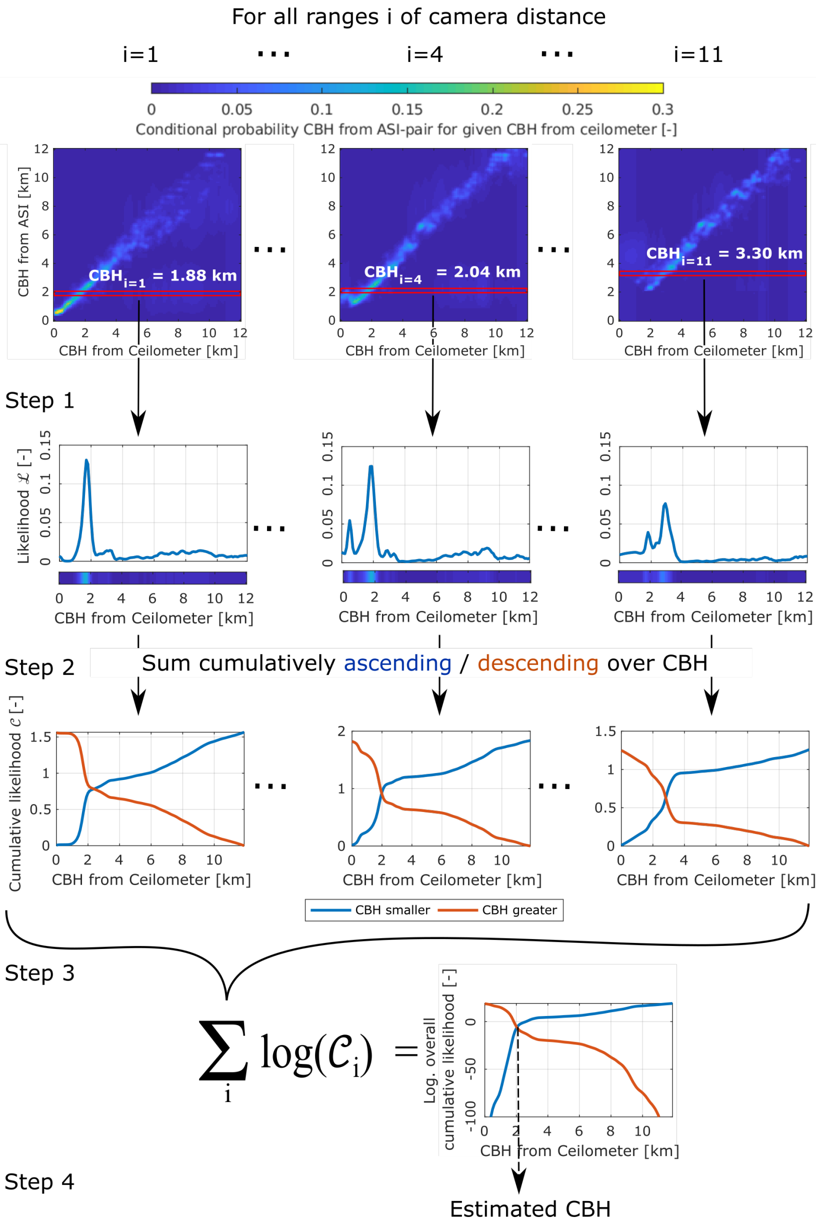

$$\sum_i \log(\mathcal{C}_i) =$$

Figure 5. Inference procedure — Step 1: For each range i of camera distance CBH_i is computed as mean CBH from the respective ASI-pairs. Conditional probability is evaluated that CBH_i would be received if true CBH (at the ceilometer) took on a value $\{0...0.1, 0.1...0.2, ..., 11.9...12\}$ km (red boxes). Step 1 yields a likelihood function for each range of camera distance. Step 2: Cumulative and complementary cumulative likelihood are calculated for each range of camera distance. Step 3: These functions are logarithmized and then summed over all ranges i of camera distance yielding overall cumulative and complementary cumulative likelihood. Step 4: The Intersection of both functions gives the estimated likeliest CBH.

the CBH which is most likely to be present. The characteristics of each ASI-pair are in the following described by conditional probability distributions, which will by retrieved in Sect. 3.4. These distributions provide the probability of receiving a certain CBH reading from an ASI-pair, given that actually a specific reference CBH is present. Our estimation procedure then uses principles from Maximum Likelihood Estimation (MLE) ~~. Figure~~and modifies them for the specific case. To the best of our knowledge, the usage of a statistical method and in particular one relying on conditional probability distributions is novel to the task of estimating CBH from the observations of a multitude of ASIs.

To give an overview, Fig. 5 shows the inference process used to estimate CBH by the network based on the 42 CBH readings provided by the individual ASI-pairs. For each range i of camera distance, ~~conditional probabilities estimated~~ in Sect. 3.4, conditional probability distributions will be estimated. These conditional probabilities are translated into the likelihood that actually certain values of (reference) CBH are present (step 1) based on the readings of CBH received ~~for~~ from ASI-pairs in this range i of camera distance. After calculating the cumulative likelihood for each range of camera distance (step 2), these are combined yielding the overall cumulative and complementary cumulative likelihood from all ~~ASIs~~ ASI-pairs (step 3). Finally, the value of CBH which is most likely to be present at the site and at the evaluated time, given the readings from all involved ASI-pairs, is estimated (step 4). These steps are ~~explained~~ presented in more detail in the following.

Step 1: For each ASI-pair, the median value of all valid CBH readings of the previous $10\ \mathrm{min}$ is calculated. If an ASI-pair does not provide any valid CBH within this period, it is excluded from the prediction for the instance in time evaluated. The ranges of camera distance $1 \ldots 2.5\ \mathrm{km}$ and $3 \ldots 4\ \mathrm{km}$ are represented by a larger number of ASI-pairs than the remaining distances. ~~To~~ Thus, the readings of ASI-pairs in these ranges of camera distance may prevail in the estimation of CBH. As the variety of camera distances is considered to bring a benefit to the procedure, we intend to represent all camera distances as uniformly as possible~~,~~. For this, we define ranges of camera distance~~are defined~~, using the range limits $\{0.5, 1, 1.5, \ldots, 6\}\ \mathrm{km}$~~and~~. CBH readings of all ASI-pairs with camera distance in range i are averaged to yield CBH_i. Consecutively, the conditional probability ~~$P(\mathrm{CBH}_i \mid \theta)$~~ $P(\mathrm{CBH}_i \mid h_{true})$ is evaluated that the found CBH_i would be received for a given true CBH ~~θ~~ h_{true} (red marked box prior to step 1 in Fig. 5). Note that ~~$P(\mathrm{CBH}_i \mid \theta)$ was~~ $P(\mathrm{CBH}_i \mid h_{true})$ will be modeled in Sect. 3.4 measuring CBH h_{Ref} by a ceilometer which ~~provided $h_{Ref} \approx \theta$~~provides $h_{Ref} \approx h_{true}$. Thus, the likelihood ~~$\mathcal{L}_i(\theta)$~~ $\mathcal{L}_i(h_{true})$ is obtained (Fig. 5, output of step 1):

$$\mathcal{L}_i(\cancel{\theta} h_{true}) = P(\mathrm{CBH}_i \mid \cancel{\theta} h_{true}). \tag{1}$$

Step 2: ~~Likelihood is~~ We define cumulative likelihood $\mathcal{C}_i(\hat{h}_{true})$ as the likelihood of receiving the present reading CBH_i given that h_{true} is smaller or equal to an estimation of true CBH $\hat{h}_{true}$. Accordingly in the implementation, likelihood is summed cumulatively over all bins of reference CBH ~~θ to define cumulative likelihood~~ h_{true} (Fig. 5, step 2):

$$\mathcal{C}_i(\hat{h}_{true}) = \sum\nolimits_{\cancel{\theta \leq \hat{\theta}} h_{true} \leq \hat{h}_{true}} \mathcal{L}_i(\cancel{\theta} h_{true}). \tag{2}$$

Likewise, a complementary cumulative likelihood is defined

$$\cancel{\bar{\mathcal{C}}_i(\hat{\theta}) = \sum_{\theta > \hat{\theta}} \mathcal{L}_i(\theta).}$$

as the likelihood of receiving the present reading CBH_i given that h_{true} is greater than an estimation of true CBH $\hat{h}_{true}$:

$$\bar{\mathcal{C}}_i(\hat{h}_{true}) = \sum_{h_{true} > \hat{h}_{true}} \mathcal{L}_i(h_{true}). \tag{3}$$

~~$\mathcal{C}_i(\hat{\theta})$ and $\bar{\mathcal{C}}_i(\hat{\theta})$ are used here as measures how likely it is that actual CBH θ is in the interval $]0\,\mathrm{km},\hat{\theta}]$ or $]\hat{\theta},12\,\mathrm{km}]$ respectively. It is mainly the~~ In particular, the use of these cumulative functions ~~that~~ and the estimation of likelihood functions from measurement data distinguishes the present approach from a regular Maximum-Likelihood-Estimation (MLE). This modification is used as in MLE typically smooth analytical ~~likelihood~~ functions are assumed as likelihood function. In contrast, likelihood functions here ~~are~~ will be estimated based on empirical conditional probabilities. These approximated likelihood-functions, derived from a dataset of finite size, may therefore be less smooth and may not be completely ~~representable.~~ representative. When using cumulative distributions, it is expected that the method still works robustly if the conditional probabilities are not estimated accurately for each grid cell of the discrete distribution if at least the cumulative value over a range of CBH is appropriate. In spite of the modification, the presented approach may adopt beneficial properties of MLE: The use of appropriate conditional probabilities (~~described~~ determined in Sect. 3.4) reduces systematic deviations of estimated CBH compared to the measurement of a single ASI-pair. Moreover, applied conditional probabilities are in general not specific to the studied site and its meteorological conditions which allows to apply the method at other sites. ~~When using cumulative distributions, it is expected that the method still works robustly if the conditional probabilities are not estimated accurately for each joint frequency grid cell but at least the cumulative value over a range of CBH is appropriate. Both functions $\mathcal{C}_i(\hat{\theta})$ and $\bar{\mathcal{C}}_i(\hat{\theta})$~~ Both functions $\mathcal{C}_i(\hat{h}_{true})$ and $\bar{\mathcal{C}}_i(\hat{h}_{true})$ are shown for three exemplary intervals of camera distance in Fig. 5 as output of step 2.

Step 3: ~~The natural logarithm is then applied to $\mathcal{C}_i(\hat{\theta})$ and summed over all~~ We aim to determine the likelihood of receiving the combination of readings CBH_i from all the intervals i of camera distance ~~to yield the~~ given that $h_{true} \leq \hat{h}_{true}$. This can be expressed as product of $\mathcal{C}_i(\hat{h}_{true})$ from all intervals i. As this product would often become zero in our numerical treatment, we instead calculate its natural logarithm, which we refer to as overall logarithmized cumulative likelihood $\log\,\mathcal{C}_n(\hat{h}_{true})$. This operation also allows to replace the product by a sum (Fig. 5, step 3)~~given the readings CBH_i per interval i of camera distance~~ :

$$\log\,\mathcal{C}_n(\hat{h}_{true}) = \sum_i \log \mathcal{C}_i(\hat{h}_{true}). \tag{4}$$

Analogously, an overall complementary logarithmized cumulative likelihood is computed given all readings CBH_i per interval i of camera distance

$$\log\,\bar{\mathcal{C}}_n(\hat{h}_{true}) = \sum_i \log \bar{\mathcal{C}}_i(\hat{h}_{true}). \tag{5}$$

Both functions are visualized exemplarily as output of step 3 in Fig. 5. ~~In theory, the method could do without the application of a logarithm to $\mathcal{C}_i$ and $\bar{\mathcal{C}}_i$ in Eq. and Eq. respectively. In that case, the sum would be replaced by a multiplication in the respective equations. However, this would induce numerical problems regularly as handled products approach zero.~~

Step 4: ~~The left hand sides in Eq. and Eq.~~ $\log\,\mathcal{C}_n(\hat{h}_{true})$ and $\log\,\bar{\mathcal{C}}_n(\hat{h}_{true})$ are only known at discrete points. Linear interpolation yields continuous representations of these. ~~An estimation of the likeliest actual CBH $\theta_{likeliest}$ is selected for which $\log\,\bar{\mathcal{C}}_n(\hat{\theta})$ and $\log\,\mathcal{C}_n(\hat{\theta})$~~ Then finally, we aim to select the true CBH $h_{likeliest}$, which makes it likeliest to receive the given combination of CBH_i. In our formulation of the problem, this means we intend to find a $\hat{h}_{likeliest}$ which simultaneously maximizes $\log\,\mathcal{C}_n(\hat{h}_{true})$ and $\log\,\bar{\mathcal{C}}_n(\hat{h}_{true})$. Consequently, we accept $h_{likeliest}$, for which $\log\,\mathcal{C}_n(\hat{h}_{true})$ and $\log\,\bar{\mathcal{C}}_n(\hat{h}_{true})$ are equal (Fig. 5, step 4):

$$\cancel{\theta}h_{likeliest} = \mathrm{argmin}_{\cancel{\hat{\theta}}\hat{h}_{true}} \left|\log\,\bar{\mathcal{C}}_n(\hat{h}_{true}) - \log\,\mathcal{C}_n(\hat{h}_{true})\right|. \tag{6}$$

Besides this estimation of CBH, a version of this procedure will be discussed that includes further refinements (in the following referred to as *refined* estimation). ~~The refinement is motivated by the finding that some~~ As a first observation from the generation of conditional probabilities, ASI-pairs ~~are already accurate if actually a certain range of CBH is present as we will discuss in Sect. 4. First, the procedure presented above is modified to exclude ASI-pairs~~ with camera distance greater than 4.5 km ~~as these ASI-pairs~~ cause large deviations for CBH < 4 km and ~~only provide a limited benefit~~ exhibit only a moderate advantage at greater CBH. ~~Results from this procedure are accepted as refined estimation $\theta_{refined}$ if estimated CBH is within 3...12 km. Otherwise, the arithmetic average of CBH measured by~~ These ASI-pairs are excluded from the refined estimation of $h_{likeliest}$. On the other hand, ASI-pairs with ~~specific camera distance is used. The most appropriate~~ small camera distance are already accurate if only small CBH occur, as we will discuss in Sect. 4. We inspected conditional probabilities of the ASI-pairs ~~for an interval of CBH are identified by an inspection of the conditional probabilities~~ (exemplarily viewed as input to step 1 in Fig. 5) ~~. This~~ and identified the ASI-pairs which are most appropriate for an interval of CBH. Based on this, the refined estimation is ~~restricted to remain within the specific interval of CBH from the unrefined estimation in which it is applied~~received from the arithmetic average of CBH measured by ASI-pairs with corresponding small camera distance, if the first iteration of $h_{likeliest}$ yielded a sufficiently small CBH. In summary, the refinement procedure to receive the final estimation of CBH ~~$\theta_{refined}$ reads~~ $h_{refined}$ reads

$$\cancel{\theta}h_{refined} \begin{cases} h_{likeliest}, & h_{likeliest} \in]3,12]\ \mathrm{km} \\ \min(3\ \mathrm{km}, \mathrm{mean}(h_{i\in\{i|d_i<1.6\ \mathrm{km}\}})), & h_{likeliest} \leq 3\ \mathrm{km} \wedge \mathrm{mean}(h_{i\in\{i|d_i<1.6\ \mathrm{km}\}}) > 1.5\ \mathrm{km} \\ \min(1.5\ \mathrm{km}, \mathrm{mean}(h_{i\in\{i|d_i<1.2\ \mathrm{km}\}})), & h_{likeliest} \leq 3\ \mathrm{km} \wedge \mathrm{mean}(h_{i\in\{i|d_i<1.6\ \mathrm{km}\}}) \leq 1.5\ \mathrm{km}. \end{cases} \tag{7}$$

3.4 Estimation of conditional probabilities of CBH (ORDER OF SECTIONS 3.3 AND 3.4 WAS EXCHANGED)

The procedure to combine CBH-measurements from independent ASI-pairs, which are organized as a network, requires knowledge of the (conditional) probability to receive a certain reading of CBH from an ASI-pair given the true CBH takes on some specific value. The ~~method itself will be presented in Sect. 3.3. Here we discuss the probability distributions used. The~~ required distribution aims to answer the following question: If true CBH ranges in between $1.8...1.9$ km, how large will be the probability that an ASI-pair with camera distance 2.2 km delivers a certain CBH e.g. within $0...0.1$ km or $1.8...1.9$ km or $11.9...12$ km? In the following, these conditional probabilities are estimated not only for the range of true CBH between $1.8...1.9$ km but for each range $\{0...0.1, 0.1...0.2, 0.2...0.3, ..., 11.9...12\}$ km of true CBH. Conditional probability distributions of this kind are not available so far for ASI-pairs. Therefore, we aim to approximate them from the measurement data of a modelling period. Estimations of CBH from the available ASI-pairs and measurements from the ceilometer during the period 01 April 2019 to 29 June 2019 are used. CBH measured by the ceilometer serves as reference CBH. It is considered not to be essential that the training period is representative of the period to which the method is applied. However, we expect that the method works best if the included ASI-pairs exhibit a similar distribution of measurement deviations given the same reference CBH in both periods. For solar applications and the latitude of this study, we consider the used dataset and its split reasonable. The summer and shoulder months provide the main share of the annual solar yield at the site and are therefore in the focus of the nowcasting system under development. In that sense, the training dataset is considered to be for the large part representative of conditions relevant to solar applications at similar latitudes.

The seven ASIs available in the urban area are arranged into 42 ASI-pairs. Each tuple of two ASIs, that is selected from the set of seven ASIs, yields 2 independent ASI-pairs by swapping the ASI used as main camera (see Sect. 3.1).

The procedure is developed based on periods in which valid measurements from ceilometer and the respective ASI-pair are available and in which the variability of CBH is moderate: For each time stamp a window of 30 min centered at this time stamp is defined. A time stamp is only included if standard deviation of reference CBH within the window is less than 30% of the mean value of reference CBH within the same window. As discussed before, ASI-pairs and ceilometer measure CBH as spatial median and point-wise respectively. Therefore, this filter intends to assure that ceilometer and ASI-pair measure CBH of the same layer. CBH from the respective ASI-pair and from the ceilometer are processed by a moving-median filter with a window of 10 min. The joint frequency distribution of CBH measured by ceilometer h_{Ref} and the respective ASI-pair h_{ASI} is computed from these simultaneously acquired time series. ~~That means the~~ In other words, the domain of reasonable values, $[0, 12\ \mathrm{km}[\times[0, 12\ \mathrm{km}[$, which the pair (h_{Ref}, h_{ASI}) can take on, is discretized into a mesh of square grid cells with side lengths Δh. Then the frequency is calculated with which (h_{Ref}, h_{ASI}) is observed in ~~a discrete grid cell defined by the interval $[j\Delta h, (j+1)\Delta h[$ for h_{Ref} and the interval $[k\Delta h, (k+1)\Delta h[$ for h_{ASI}, where $j, k \in \{0, 1, 2, ..., N-1\}$~~ each of the discrete grid cells. A bin size $\Delta h = 100$ m is chosen in a trade-off between sources of error. Finer bins will allow to represent the distributions at higher resolution and will thus allow for higher resolved measurements of CBH in the network. However, the size of the used data set is limited which makes it difficult to model these distributions at highest resolution. The bin size chosen here is expected to limit the achievable uncertainty of the measurement to a minimum level of 100 m. ~~Joint frequency distributions modeled here are restricted to a maximum CBH of 12 km. This yields $N = 120$.~~

Joint frequency distributions were inspected and found to be well reproduced among the studied independent ASI-pairs, if only the corresponding camera distances are similar. This meets the expectation from literature discussed in Sect. 3.1. Moreover, we conclude that the distributions modeled here will be transferable to other setups that use camera distances in the studied range. Local climate is expected to influence the transferability to a minor extent~~as will be discussed later. To further support this transferability to~~.

The limited size and representativeness of the data set used in model development are expected to cause random features in the joint frequency distributions which are not useful to the estimation procedure, when it is applied to other setups, sites and times ~~, we aim to suppress~~ (such as represented by the validation data set). To suppress such random features of received joint frequency distributions~~. For this , the original joint frequency distribution F_l of ASI-pair l is transformed by a first filter into $F_{l,filter\ 1}$ and by a consecutively applied filter into $F_{l,filter\ 2}$.~~ , we introduce a filtering procedure with two consecutive steps described here and in more detail in Appendix A. The parameter values set in the filtering procedure are approximate to this point and are based on a visual comparison of unfiltered and filtered distributions, evaluating the degree to which noise but also reasonable features were suppressed. The parameters values may be optimized in a future study.

First, a weighted mean filter is applied between the original joint frequency distributions ~~F_l received from all~~ received for ASI-pairs with ~~arbitrary camera distance d~~

$$F_{l,filter\ 1} = \frac{\sum_j w_{l,m} F_m}{\sum_j w_{l,m}}.$$

~~For the joint frequency distribution F_l of each respective ASI-pair l, weights $w_{l,m}$ are used that include~~ similar camera distance. As discussed above, ASI-pairs with similar camera distance ~~. More precisely, a triangular window, based on the difference of camera distance $\Delta d_{l,m}$ of ASI-pair m compared to ASI-pair l, is used that is defined by~~

$$w_{l,m} = max(0, 1 - \Delta d_{l,m}/0.5\ \mathrm{km}).$$

~~Then~~ are expected to perform similarly in the measurement of CBH and should consequently also exhibit similar joint frequency distributions of CBH. Thus, the filter aims to suppress differences between the joint frequency distributions of ASI-pairs which may result from disturbances in the estimation rather than from a difference in the systems' characteristics.

To each filtered distribution resulting from the prior step, a composite of three Gaussian filters is applied~~to $F_{l,filter\ 1}$ of each ASI-pair l~~. We first decompose each distribution ~~$F_{l,filter\ 1}$~~ by conditional filters into three separate *modes*~~. In the second step~~, which correspond to parts of the joint frequency distributions which are estimated with descending precision. Thereafter, we apply ~~to each mode~~ a Gaussian filter ~~g_σ with distinct standard deviation σ_{mode}~~ to each mode. The standard deviation of the Gaussian ~~kernel. The subscript *mode* indicates the specific mode for which σ_{mode} is applied.~~ filter applied to each mode corresponds qualitatively to the uncertainty with which the prior joint frequency distribution is estimated within grid cells of that mode. Consecutively, the three filtered modes are summed to receive the smoothened joint frequency distribution.

The first mode is constituted by ~~all outlier observations. Outliers are defined here as grid cells (h_{Ref}, h_{ASI}) for which~~ grid cells for which the ASI-pair based measurement of CBH ~~h_{ASI}~~ deviates by more than 1.5 km from the ceilometer reading~~h_{Ref}:~~

$$F_{l,outlier}(h_{Ref}, h_{ASI}) = \begin{cases} F_{l,filter\ 1}(h_{Ref}, h_{ASI}), & |h_{ASI} - h_{Ref}| > 1.5\ \mathrm{km} \\ 0, & \text{else.} \end{cases}$$

~~Such outliers will contain a large random component. We expect that in a reproduction of the experiment, a similar number of outliers will be received, while~~ . The large deviations represented by this mode occur less frequently which is why the joint frequency distribution will be estimated less precisely for the respective grid cells. On the other hand, apart from such scattering effects, the joint frequency ~~found for a single grid cell (h_{Ref}, h_{ASI}) may vary significantly. Therefore, the strongest filter~~ distributions are found to be comparably smooth in the grid cells of this mode. A Gaussian filter with a large standard deviation of $1\ \mathrm{km}$ is applied to this mode ~~using $\sigma_{outlier} = 1\ \mathrm{km}$.~~ which is considered to be apt to preserve the expected distribution while suppressing random features.

The second mode is constituted by grid cells ~~that are not part of the first mode and~~ for which the ASI-pair based measurement of CBH deviates by less than $1.5\ \mathrm{km}$ from the ceilometer reading and which feature a joint frequency ~~less than the average over~~ below the average of all grid cells~~of the joint frequencydistribution:~~

$$F_{l,inconfident}(h_{Ref}, h_{ASI}) = \begin{cases} F_{l,filter\ 1}(h_{Ref}, h_{ASI}), & |h_{ASI} - h_{Ref}| \leq 1.5\ \mathrm{km} \\ & \wedge\ F_{l,filter\ 1}(h_{Ref}, h_{ASI}) < \mathrm{mean}(F_{l,filter\ 1}) \\ 0, & \mathrm{else.} \end{cases}$$

~~The~~. These grid cells typically exhibit a larger joint frequency, i.e. more observations, than grid cells in the first mode. Still the comparably small number of observations in these grid cells is expected to cause an increased uncertainty of the estimated joint frequencies. ~~For this mode, $\sigma_{inconfident} = 0.5\ \mathrm{km}$~~ Consequently in a trade-off between suppressing random scattering and preserving meaningful variations a Gaussian filter with standard deviation $0.5\ \mathrm{km}$ is applied.

The third mode ~~$F_{l,confident}(h_{Ref}, h_{ASI})$~~ makes up the complementary of the first and second mode. It contains grid cells that are observed with an at least average joint frequency and which are not classified as outliers~~:~~

$$F_{l,confident}(h_{Ref}, h_{ASI}) = \begin{cases} F_{l,filter\ 1}(h_{Ref}, h_{ASI}), & |h_{ASI} - h_{Ref}| \leq 1.5\ \mathrm{km} \\ & \wedge\ F_{l,filter\ 1}(h_{Ref}, h_{ASI}) \geq \mathrm{mean}(F_{l,filter\ 1}) \\ 0, & \mathrm{else.} \end{cases}$$

. Joint frequencies in these grid cells are considered to ~~have~~ be estimated with a comparably high accuracy. To avoid a loss of precision and ultimately a loss of accuracy in the estimation of CBH, a ~~small value of $\sigma_{confident} = 0.1\ \mathrm{km}$~~ Gaussian filter with a standard deviation of $0.1\ \mathrm{km}$ is used. ~~The three filtered modes g_σ are summed to receive the smoothened joint frequency distribution~~

$$F_{l,filter\ 2} = g_{\sigma_{outlier}}(F_{l,outlier}) + g_{\sigma_{inconfident}}(F_{l,inconfident}) + g_{\sigma_{confident}}(F_{l,confident}).$$

Hence, only neighboring grid cells have a significant influence on this filter.

In many joint frequency distributions, there are grid cells with joint frequency close to zero. Especially for these grid cells, a greater ~~dataset~~ data set would be required to receive more representative values. For all grid cells, joint frequency is increased to a minimum value of 0.5 to avoid underestimations of joint frequency. This value corresponds to half of the joint frequency associated with a single actual observation in a grid-cell. For the estimation procedure of CBH, ~~this~~ such a minimum value leads to slightly reduced precision for most readings but increased robustness in the case that these grid cells (h_{Ref}, h_{ASI}) are indeed observed in the measurement.

~~Finally,~~ Finally, from each joint frequency distribution~~is normalized with the sum of all joint frequency grid cells. In this way, a probability mass function (also known as discrete density function) to measure a certain CBH with the respective ASI-pair and to coincidentally measure a certain CBH with the ceilometer is yielded. The~~ , the conditional probability $P(h_{ASI} \mid h_{Ref})$ to receive a certain CBH reading from an ASI-pair, given that the ceilometer measures some certain CBH, is ~~calculated by dividing the respective probability mass function by the marginal distribution of CBH measured by the ceilometer. The latter distribution gives the probability to receive CBH from the ceilometer within a certain bin h_{Ref} regardless of which CBH reading is simultaneously received from an ASI-pair. The distrbution can be derived from any of the probability mass functions by summing all grid cells of the probability mass function which correspond to the respective bin h_{Ref} of CBH measured by the ceilometer.~~ derived (see Appendix A for a more detailed description).

~~Inference procedure — Step 1: For each range i of camera distance CBH$_i$ is computed as mean CBH from the respective ASI-pairs. Conditional probability is evaluated that CBH$_i$ would be received if true CBH (at the ceilometer) took on a value {0...0.1,0.1...0.2,...,11.9...12} (red boxes). Step 1 yields a likelihood function for each range of camera distance. Step 2: Cumulative and complementary cumulative likelihood are calculated for each range of camera distance. Step 3: These functions are logarithmized and then summed over all ranges i of camera distance yielding overall cumulative and complementary cumulative likelihood. Step 4: The Intersection of both functions gives the estimated likeliest CBH.~~

The inference procedure, which ~~is~~ was introduced in Sect. 3.3, represents each range i of camera distance bounded by the limits $\{0.5, 1, 1.5, ..., 6\}$ km by a single distribution of conditional probability. For each range of camera distance, the distribution of conditional probability, which corresponds to the camera distance closest to the center of this range, is selected ~~. For example , for the range $i = 2$ representing camera distances 1...1.5 km, the center of the range would be 1.25 km. For the camera distances 1.081, 1.247 and 1.352 km, conditional probabilities have been modeled. Consequently, for this range of camera distance, the distribution of conditional probability corresponding to the camera distance 1.247 km is used.~~ (example provided in Appendix A). Figure 5 (above Step 1) shows exemplary conditional probabilities for three ASI-pairs with camera distances $0.8,\ 2.2,\ 5.7$ km representing the ranges of camera distance $i = 1,\ 4,\ 11$ respectively. ~~The further content of Fig. 5 is explained in the next section~~BIAS and precision, with which ASI pairs of distinct camera distances measure CBH, given a certain reference CBH, are visible in these conditional probabilities. Such characteristics will be evaluated in more detail in the following, based on a separate validation data set.

4 Validation of CBH measurement by the ASI network and comparison to CBH measurements by the ASI-pairs

In this section, the accuracy of CBH measurement by the ASI network and by 42 independent ASI-pairs set up at a wide variety of camera distances and alignments is compared. This section is based on a validation data set including the days from 30 June 2019 to 27 September 2019. This dataset was excluded from the model development described in Sect. 3. The analyzed quantity is 10 min-median CBH. ~~The evaluations are restricted to times in which the variability of CBH is small. More precisely, the standard deviation of CBH within a window 15 min before and after the analyzed time is required to be less than 30% of mean CBH within the same window. As discussed above, the ASI-pairs and the ASI network are expected to~~

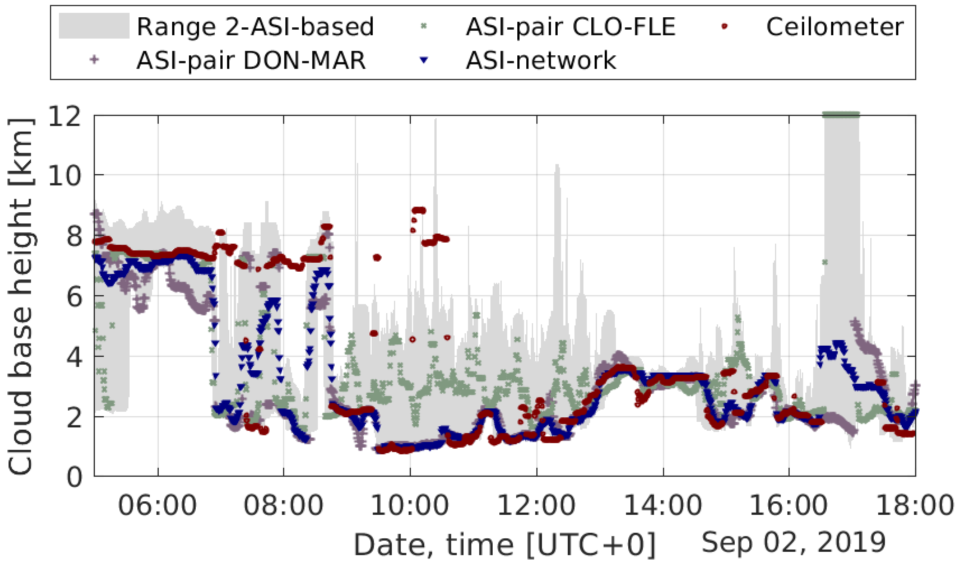

Figure 6. Time series of cloud base height for ~~two~~ an exemplary ~~days~~ day (02 September 2019) measured by 42 ASI-pairs (grey filled), by two exemplary ASI-pairs DON-MAR and CLO-FLE with respective camera distances 0.8 and $4.2\ \mathrm{km}$, by the ASI network with refinements and by a ceilometer in the urban area of Oldenburg.

~~measure a spatial median CBH whereas the ceilometer measures CBH at the point of its installation. This restriction aims to assure comparability of both measurements.~~

First, characteristics of CBH-measurements from the ASI network and from individual ASI-pairs are compared to the CBH-measurement of the reference ceilometer based on insightful days. Then, the ~~coincidence of CBH , measured~~ measurements of CBH by ASI network and ASI-pairs ~~with CBH measured by the ceilometer, is analyzed~~ are compared to the one of the ceilometer by scatter-density plots. Subsequently, ~~CBH derived by the network and by all individual ASI-pairs are validated against the ceilometer by RMSD and BIAS~~the accuracy of an ASI-pair and of the ASI network are analyzed for the application of nowcasting of solar irradiance. Finally, ~~these deviation metrics received~~ deviation metrics of CBH received from the network and from all individual ASI-pairs per interval of CBH are discussed.

4.1 Comparison of CBH measurements for ~~two~~ an exemplary ~~days~~day

~~Figure 6 bottom~~ We first analyze the properties of the different procedures to measure CBH based on exemplary situations. Fig. 6 visualizes time series of CBH for a variable day (02 September 2019) measured by ceilometer, by all available ASI-pairs and by the ASI network. The time series of two exemplary ASI-pairs DON-MAR and CLO-FLE with respective camera distances 0.8 and $4.2\ \mathrm{km}$ are plotted. The range of CBH-readings covered by all available ASI-pairs is shaded grey in the figure. ~~The day features a high cirrus cloud layer which is later obscured by a low cumulus cloud layer. Occasionally, the low layer opens and the high layer is observed. Towards the evening, the sky becomes mostly clear.~~

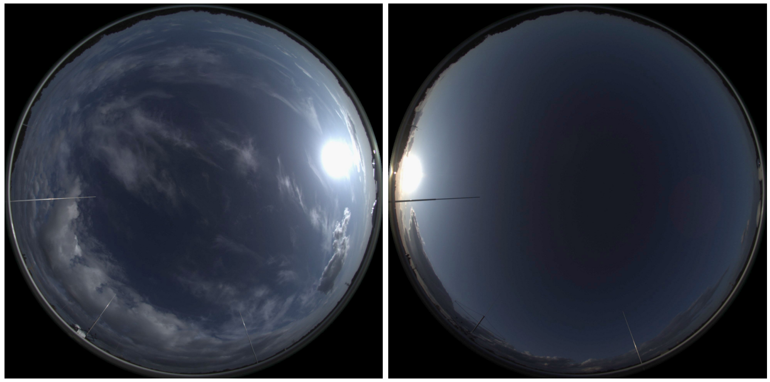

Figure 7. Sky images taken by ASI UOL representing ~~multi-cloudlayer situations~~ a multi-cloud-layer situation on ~~06 August 2019 12:35 (left) and on~~ 02 September 2019 7:20 (~~center~~left) and an almost clear-sky situation on 02 September 2019 17:00 (right) respectively.

In the morning (06:00), both ceilometer and the ASI network recognize adequately a high cloud layer. The ASI-pairs with valid measurements deliver similar estimations of CBH. Around ~~(~~07:00~~)~~, the ceilometer still recognizes the high layer whereas many ASI-pairs as well as the ASI network recognize the approaching cumulus clouds. These already cover a significant fraction of the sky in the urban area (compare Fig. 7, ~~center~~left). The CBH estimation approach tends to react stronger to clouds in this area of the sky in which contrasts are typically pronounced. Around 10:20 a multilayer situation is present. In the whole sky dome cumulus clouds are visible but a large fraction of the cloud cover is made up by the cirrus layer. Around this time the measurements of ceilometer and ASI network coincide well. All ASI-pairs recognize a rather low cloud layer while there are periods in which the ceilometer recognizes the cirrus layer. All of the ASI-based CBH estimations react stronger to the low layer and miss the high layer clouds. These two situations impress well why the ASI-based estimations of CBH are less accurate for higher clouds and tend to be negatively biased. On the other hand, for low clouds a high accuracy of the combined CBH estimation is demonstrated.

Meanwhile, it is visible that, for low clouds, many ASI-pairs such as ASI-pair CLO-FLE, tend to overestimate CBH. In these conditions, the ASI network manages well to follow appropriate estimations.

Around 17:00, a nearly clear sky is visible (compare Fig. 7, right). Consequently, the ceilometer does not provide any valid CBH. The ASI-pairs provide a CBH that scatters over a wide range, while the ASI network provides ~~a CBHthat is assumed to be reasonable. The~~ an intermediate CBH. A similar reading of CBH is also recognized by a fraction of the ASI-pairs. From around 17:05, the ASI network detects a CBH of 3 km. With 3.1 km, the following CBH measurements of the ceilometer around 17:~~30~~ 25 confirm the suggested CBH of the approaching cloud layer ~~.~~ (see Fig. B1 for a detail view of the CBH measurements during this almost clear sky period). This situation reflects the expected behavior of the ASI network under mostly clear conditions. However, for a completely clear sky, the ASI network partly produces invalid readings (NaN) and partly it detects a large CBH of around 10 km. In this case, a consecutive image processing step detects the absence of clouds. This step is not part of the present study.

~~Figure 6 top shows CBH on 06 August 2019 again measured by ceilometer, by all available ASI-pairs and by the ASI network. This day, similar to 02 September 2019, discussed previously, includes multi-layer conditions with high layers overlaid by low layers, resulting in similar observations. In the morning and evening high cloud layers are dominant. The CBH of these varies in the range of 7...11 km according to the ceilometer. The range of CBH from ASI-pairs reflects this spread. Still, it is not obvious which of the ASI-pair based observations would be the most appropriate. From the ASI network a rather steady CBH estimation results which most of the time reflects the dominant CBH layer as recognized by the ceilometer. The combined estimation misses physically meaningful variations of CBH typically towards higher values recognized by the ceilometer. Also for this day time series of CBH and corresponding ASI images were compared. Again large underestimations of CBH by the ASI network (at 05:30, 08:15, 10:00, 12:30, 16:00) were traced back to the ASI-based estimations responding stronger to lower optically denser low cloud layers which pass the vicinity of the urban area (compare Fig. 7, left).~~

The time series of CBH from DON-MAR and CLO-FLE demonstrate the properties of ASI-pairs with respectively small and large camera distance. DON-MAR is typically close to the reference CBH if it actually takes on a value below 4 km (e.g. 02 September 2019 9:00...13:00) while this ASI-pair tends to take on large deviations and a negative BIAS for larger CBH (e.g. 02 September 2019 6:00...9:00). ASI-pair CLO-FLE typically misses the CBH of low clouds and provides a significantly overestimated CBH (e.g. 02 September 2019 9:00...13:00). For high clouds, however, CBH measured by CLO-FLE often coincides well with the reference. ~~However, for CLO-FLE as in general for the ASI-pairs high layer clouds are missed if low layer clouds are present (e. g. 02 September 2019 6:00...9:00).~~ To give further insight, in Appendix B2, timeseries of CBH from the different sources are compared for another exemplary day.

4.2 Comparison of CBH measurements by relative frequencies

~~In the following deviations found for two~~ Deviations found for the exemplary ASI-pairs DON-MAR and UOL-HOL with camera distances of 0.8 km and 5.7 km as well as for the ASI network, ~~with and without~~ without and with the refinements described in Sect. 3.3, are now analyzed with the help of scatter-density plots provided in Fig. 8. The plots visualize the relative frequency of CBH measured by the respective ASI-based systems given a CBH measured by ceilometer. Thus, relative frequencies in each of the columns add to one. The plots also include the median (red dotted), limits to the interquartile range (IQR, red dashed) and 5−, 95−percentiles (red solid line) based on floating 1000 m-bins of CBH from the ceilometer. Each of the subplots further indicates performance metrics of the individual systems: Root mean squared deviation (RMSD), BIAS and coefficient of correlation (ρ).

4.2.1 ASI-pairs

The readings of ASI-pair DON-MAR, (Fig. 8 upper row, left) ~~with camera distance 0.8 km exhibits significant scattering of the CBH readings. Additionally, CBH from the~~ are well aligned with the main diagonal up to a reference CBH of around 4 km. As reference CBH increases further, the ASI-pair increasingly underestimates CBH, indicated e.g. by the median. On the contrary, ASI-pair UOL-HOL (Fig. 8 upper row, right), overestimates CBH massively if reference CBH decreases below 3 km. Whereas based on the median-value, its readings are well aligned with the reference at larger CBH.

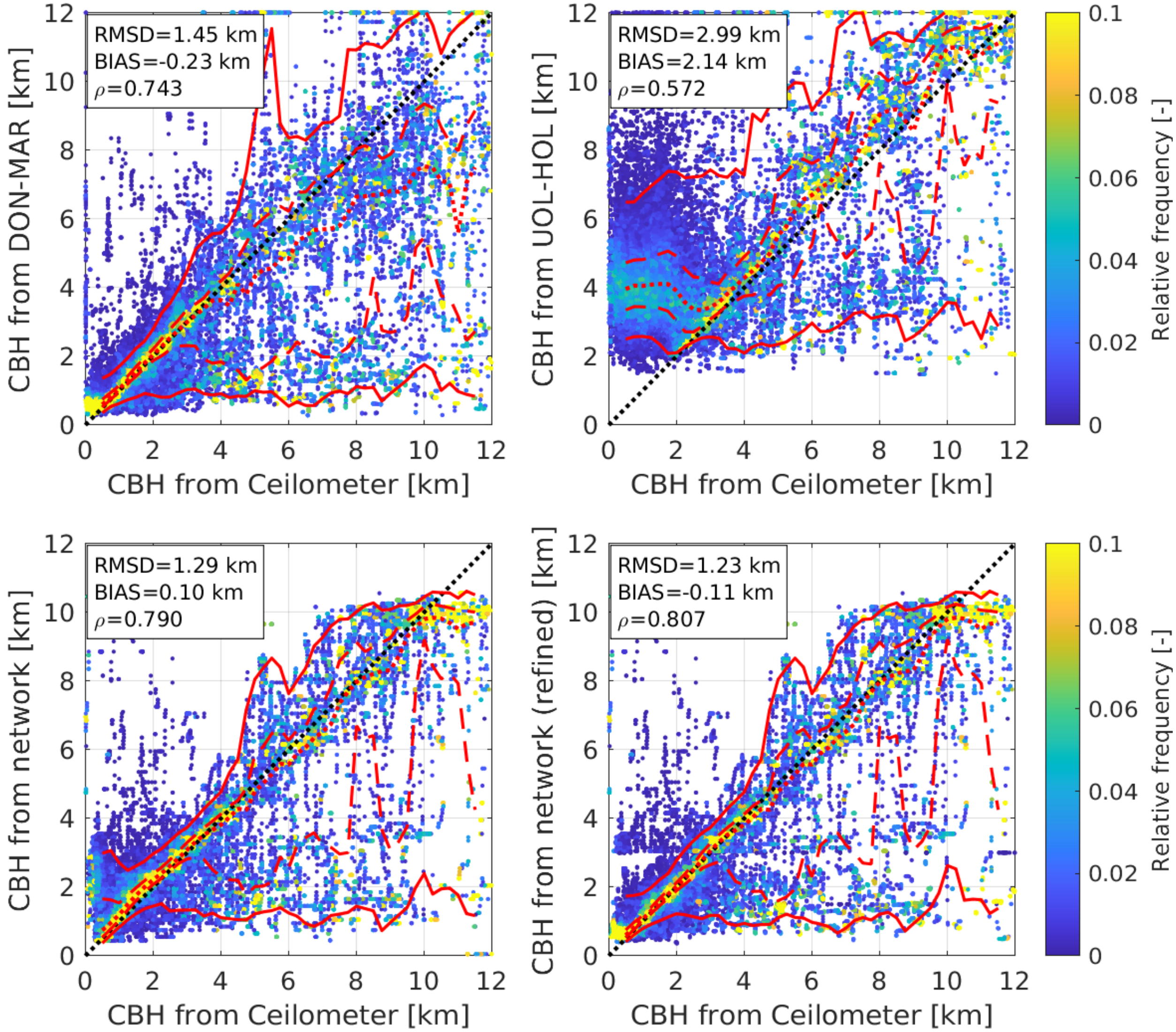

Figure 8. Relative frequency of ASI-based CBH estimation for given CBH from ceilometer~~–~~. Evaluation for two of the ASI-pairs DON-MAR (upper row, left) and UOL-HOL (upper row, right) with respective camera distances of 0.8 and 5.7 km, and from the ASI network without (bottom row, left) and with refinements (bottom row, right). Relative frequency in each column adds up to 1. Additionally, median (50%-quartile, red dotted), limits to the interquartile range (IQR, red dashed) and $5-$,$95-$percentiles (red solid line) based on floating 1000 m-bins of CBH from ceilometer are plotted.

Both ASI-pairs exhibit a strong scattering of the measurements, clearly visible from the wide spread of the quartiles as well as of the $5-$, $95-$percentiles. In agreement with the prior finding, DON-MAR is rather precise at low CBH ($\lesssim 3$ km), whereas UOL-HOL is notably more precise at greater CBH. CBH from the ASI-pairs often deviates towards ~~very low CBH. This~~

~~feature is in part also seen for the ASI network (Fig. 8 bottom row)~~low CBH, when the ceilometer measures CBH in the range 3...12 km. In this range, the 5-percentile of ASI-based CBH increases only slightly with reference CBH and comparably large relative frequencies are found close to the 5-percentile. As discussed ~~before~~in Sect. 4.1, this can ~~in part~~ result from low cloud layers which are actually present in the ASI-pairs' field of view but not at the ceilometer's location. ~~Towards high readings of the reference (≥ 8 km) DON-MAR underestimates CBH for most readings.~~

~~CBH measured by ASI-pair~~

Qualitatively, the effects seen meet the expectation from the literature (Nouri et al., 2019a; Kuhn et al., 2019; Nguyen and Kleissl, 2014). ASI-pairs with large camera distance are expected to be more accurate when measuring the CBH of high clouds. On the other hand, ASI-pairs with large camera distance are expected to be less accurate for small CBH values and are expected to exhibit a larger *minimum CBH*, below which no physically meaningful readings are received. From the geometric considerations in Sect. 3.1, a minimum CBH of about $0.18 \times d$ was expected. Where d is the camera distance. For UOL-HOL, ~~which has a camera distance of 5.7 km, is visualized in Fig. 8 upper row, right. CBH measured by UOL-HOL scatters~~ a significantly larger minimum CBH of about 2 km is evident. If reference CBH is smaller than 2 km, the ASI-pair yields measurements of CBH which scatter randomly around a ~~modus value of 3.8 km for reference CBH < 1.8 km. If reference CBH ranges between 1.8...3 km, this behavior is still observed for a significant part of the readings. For UOL-HOL nearly no reading of less than 1.5 km is recognized. In general, strong scattering is seen for this ASI-pair. However, towards large values of reference CBH the measurement appears to scatter to a smaller extent and especially for very large CBH (> 8 km) a satisfying agreement of CBH from ASI-pair and ceilometer is seen.~~ median value of 4 km. This behavior can be explained as the matching procedure fails if pattern are matched which are located at a larger zenith angle than a maximum value. Consequently, random features observed under a zenith angle smaller than the maximum value are often matched erroneously which yields a too large estimation of CBH. Similarly for DON-MAR a minimum CBH of around 0.3 km is suggested.

~~The measurement of CBH by the ASI network without refinements is shown in~~Overall, the ASI-pairs are characterized by a minimum CBH in the range of $0.32 \times d$. As described above, this suggests that the matching procedure of the ASI-pairs almost always fails if matched windows cover zenith angles larger than 67°. Further, also for reference CBH close to this minimum CBH, the ASI-pairs yield increased deviations, e.g. below 0.5 km and 3 km for DON-MAR and UOL-HOL.

4.2.2 ASI network

Based on Fig. 8 bottom row, left~~. The modus of the relative frequency distributions is~~, the ASI-network without refinements succeeds to combine the preferred properties of ASI-pairs with distinct camera distances. The median values of the ASI network are well aligned with the main diagonal for ~~most reference CBH~~ a reference CBH in the range 0.5...10 km. As indicated by the quartiles, the ASI network's precision is similar to that of an ASI-pair with small camera distance, such as DON-MAR, for reference CBH ≤ 4 km. For larger CBH, the network's precision is closer to the one of an ASI-pair with large camera distance, such as UOL-HOL. ~~Additionally, outliers are less frequent and occur with smaller deviations compared to the ASI-pairs discussed before. The ASI networkreturns no reading of CBH of more than 10.9 km. Thus, CBHis underestimated if a corresponding reference CBH is present~~

In the range of reference CBH > 10 km, the ASI network constantly returns CBH of around 10 km. In the studied climate~~(see Fig. 4) and accordingly in the dataset used for modelling readings of~~ , reference CBH in this range are comparably rare ~~. Therefore, conditional probabilities used in the estimation are modeled inaccurately. The estimation procedure uses cumulative . Compared to the usage of likelihood , this avoids frequent strong~~ (see Fig. 4). Therefore, corresponding grid cells of the conditional probability distributions, used by the estimation procedure, were approximated coarsely based on a small number of observations. The ASI network's combination method using cumulative likelihood is intended to avoid deviations resulting from these inaccuracies and ~~yields~~ thus to yield a more conservative ~~but in this case biased estimation of CBH~~estimation. However, this approach also suppresses the estimation of extreme CBH readings, which causes a BIAS under these conditions. For the analyzed site, deviations found in this range of CBH are of minor importance. ~~For low values of reference CBH ASI network and ASI-pair DON-MAR both appear to perform similarly at high accuracy. Only for~~

For very low values of reference CBH (especially ~~$CBH < 0.5$ km) with~~ $CBH < 0.3$ km) the ASI network ~~a large share of strong deviations is recognized. This deviation is connected to~~ without refinements overestimates CBH drastically. None of the ~~minimum CBH which is indicated as mentioned~~ ASI-pairs used has a sufficiently small minimum CBH for this range. We expect that the ASI network's accuracy would be enhanced significantly, especially in this range, if ASI-pairs with smaller camera distance than 0.8 km were added.

To improve shortcomings connected to conditions with very low clouds ($CBH < 1$ km), the refinements introduced in Sect. ~~4.1 for UOL-FLE but also for any other ASI-pair. Minimum CBH will be further detailed in the following section.~~ 3.3 are applied. As indicated by Fig. 8 bottom row, right, these refinements significantly improve the ASI network's performance for reference $CBH < 2$ km. In this range, the ASI network behaves for the greatest part like ASI-pairs ~~with a very small minimum CBH are underrepresented in the set of available ASI-pairs: The smallest minimum CBHis provided by ASI-pairs~~ DON-MAR and ~~MAR-DON ranging at 0.5 km. Thus, the estimation of CBH from the ASI network is dominated by ASI-pairs which are not capable to cover the range of very small CBH.~~ MAR-DON. The refinements do not affect the statistics notably for reference $CBH \geq 2$ km. Overall, this evaluation indicates that the ASI network performs significantly better than an individual ASI-pair, especially if the whole range of studied reference CBH 0...12 km should be covered. This is also indicated by the performance metrics shown in Fig. 8.

~~To meet these shortcomings, refinements to~~

4.3 CBH accuracy under nowcasting conditions

The procedure to estimate CBH, developed here, will be used as part of a nowcasting system. In this application, it is of special interest to be aware at any time which accuracy can be expected from a specific reading provided by the ~~procedure have been proposed~~ ASI-network. For this purpose, Fig. 9 shows the relative frequency of CBH measured by the ceilometer given a specific ASI-based estimation of CBH. In each row, the frequencies add up to one. It should be noted, that the performance indicated by this evaluation is more dependent on the local cloud conditions than the one in Sect. ~~3.3. With these adaptions the CBH measurements shown in Fig. 8 bottom row, right are received. The adaptions noticeably affect measurements if reference CBH is smaller than 3 km and most pronouncedly if reference CBH is smaller than 0.75 km. In the latter range~~ 4.2. We analyze

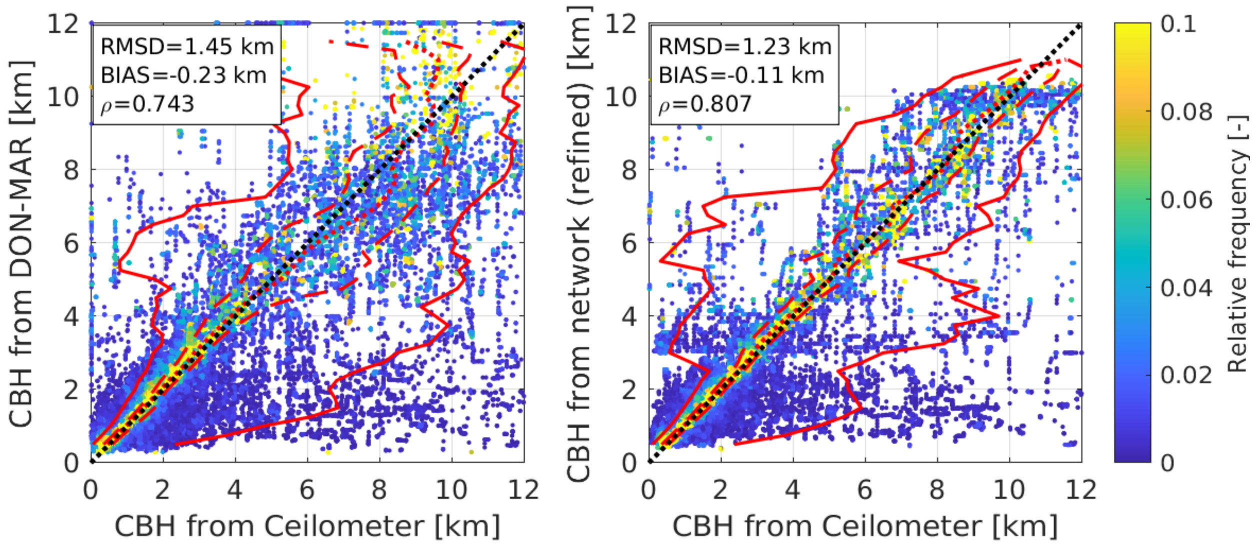

Figure 9. Relative frequency of CBH from ceilometer for given ASI-based CBH estimation. Evaluation for ASI-pair DON-MAR (left) and for the ASI network with refinements (right). Subplots (left,right) are created analogously to Fig. 8 (top, left and bottom, right). However, relative frequencies add up to one in each *row* not column.

the systems which are best in class: ASI-pair DON-MAR (Fig. 9, left) and the ASI-network with refinements (Fig. 9, right). As in the previous section, the plots also include the median (red dotted), limits to the interquartile range (IQR, red dashed) and $5-$, $95-$percentiles (red solid line) based on floating 1000 m-bins of ASI-based CBH.

Under most conditions included in Fig. 9, median and interquartile range indicate a good alignment of the CBH estimation from the ASI-network and of CBH from the ceilometer. For ASI-pair DON-MAR, a notable negative BIAS is indicated if the ASI-pair returns a CBH of 9 km or more. Also, if a CBH of more than 4 km is detected, the interquartile range indicates a notably increased precision of the ASI network~~behaves for~~. The range between the $5-$, $95-$percentiles is wide for both systems. For a wide range of CBH-readings, 5% of the estimations of CBH may deviate by more than 4 km and 3 km from the ceilometer measurement in the case of the ASI-pair and the ASI network, respectively. Still, this range is notably narrower for the ~~greatest part like ASI-pairs DON-MAR and MAR-DON. Concurrently, the~~ ASI network~~keeps its advantages over these ASI-pairs for larger CBH as described above.~~.

Based on Fig. 9, both systems are considered suited for an application in nowcasting at the studied site, while a considerable uncertainty is present. The ASI-network provides a notably improved accuracy in particular in cases when clouds at a CBH >4 km are detected.

4.4 Comparison of CBH accuracy for a three-month data set

Table 1. Frequency of measurements from the validation data set (period 30 June 2019 to 27 September 2019) per range of cloud base height (CBH) used in the evaluations described in Sect. ~~4~~4.4 (retained) and frequency of those filtered from the evaluation due to increased variability of CBH (rejected).

CBH range [km]	~~Number of observations~~Observations retained	Observations rejected
$0 < \mathrm{CBH} \leq 1$	11844	13255
$1 < \mathrm{CBH} \leq 2$	14130	9120
$2 < \mathrm{CBH} \leq 4$	9962	5923
$4 < \mathrm{CBH} \leq 8$	5559	3570
$8 < \mathrm{CBH} \leq 12$	4935	1355

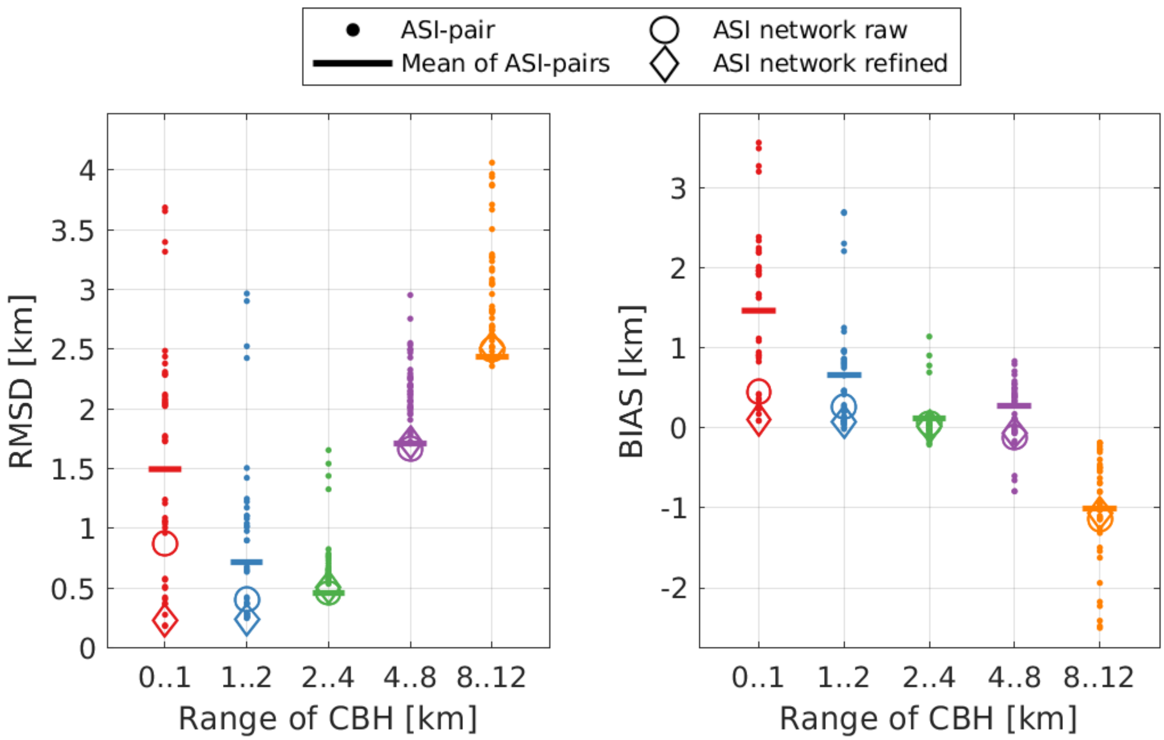

Figure 10. RMSD (left) and BIAS (right) for five ranges of CBH received for all individual ASI-pairs (dots), for the ASI network without (circles), with refinements (diamonds) and for a basic average of CBH measured by all ASI-pairs (horizontal line).

The statistical evaluations are now restricted to times in which the variability of CBH is small. More precisely, the standard deviation of CBH within a window 15 min before and after the analyzed time is required to be less than 30% of mean CBH within the same window. As discussed above, the ASI-pairs and the ASI network are expected to measure a spatial median CBH whereas the ceilometer measures CBH at the point of its installation. This restriction aims to assure a good comparability of both measurements. Further, this way our results are more comparable to a prior study by Kuhn et al. (2019).

Accuracies of CBH measurement by ASI-pairs and ASI network are analyzed separately for five ranges of reference CBH defined by the bounds $\{0,\,1,\,2,\,4,\,8,\,12\}$ km. The number of CBH measurements included in this evaluation is given in Table 1 for each of these ranges. The interval bounds are spaced irregularly to correspond better to the distribution of CBH at the site (see also Fig. 4). Table 1 also shows the number of observations excluded from the validation as significant temporal variability of CBH was detected for these observations. While a significant fraction of the readings is sorted out, the representation of the CBH ranges remains widely comparable to the original data set (see Fig. 2, left). Only the range of lowest CBH < 1000 m is represented by a notably smaller share of the validation data set.

4.4.1 Accuracy of the ASI network and ASI-pairs

Figure 10 compares RMSD (left) and BIAS (right) for CBH estimated by the ASI network, with (diamonds) and without refinements (circles) described in Sect. 3.3, to the one estimated by all ASI-pairs (dots). ~~As implied by the findings from Sect. 4.2 the final results from the ASI network provide~~ The ASI network with refinements provides measurements of CBH that are the most accurate or at least among the most accurate ones for all conditions. In terms of RMSD the estimation from the ASI network is the most accurate for the range of $\mathrm{CBH} \in [1, 8[$ km (see Fig. 10 left). For $\mathrm{CBH} < 1$ km it is slightly outperformed by two ASI-pairs (DON-MAR, MAR-DON) as well as for $\mathrm{CBH} > 8$ km by two other ASI-pairs (UOL-CLO, CLO-UOL). ASI network-based measurement of CBH provides among the smallest BIAS for $\mathrm{CBH} < 8$ km (see Fig. 10 right). The magnitude of BIAS ranges constantly below 100 m. Only for $\mathrm{CBH} > 8$ km the ASI network independently from applied corrections yields a BIAS of roughly -1050 m that corresponds to the average BIAS of all used ASI-pairs for these conditions. This deviation ~~was traced back to~~ is probably related to situations in which the ASI-based ~~measurements of CBH missing high layer clouds in the presence of low layer clouds in Sect. 4.1.~~ estimation of CBH recognizes a low cloud layer whereas the ceilometer also recognizes a high layer when gaps in the low layer appear. Therefore, this deviation is rather related to the different nature of the measurements (spatial-median compared to point-wise).

~~RMSD (top) and BIAS (bottom) received by 42 ASI-pairs utilizing camera distances in the range of 0.8...5.7 km and by the ASI network with refinements (no camera distance applicable) for the period 30 June 2019 to 27 September 2019. Figure 11 also provides deviation metrics received from the ASI network and~~ The distance between the cameras used by an ASI-pair and the reference ceilometer were considered as an influence on the accuracy of an ASI-pair. However, for the ASI-pairs ~~but distinguishes the latter by camera distance. Metrics of~~ studied, this distance to the validation site is not confirmed as a significant influence on received accuracy. This was expected in part from the ~~ASI network, with refinements, are given by horizontal lines. For small CBH (CBH < 4 km) camera distance clearly influences accuracy measured by RMSD and BIAS causing these metrics to increase steadily with camera distance. Apart from this influence metrics of the studied~~ assumption that the ASI-pairs ~~are very similar in this range of CBH~~measure the median CBH of the most dominant cloud layer in terms of features, driven by area and optical thickness.

~~For intermediate and large CBH (4...12 km) the correlation of camera distance and accuracy is not as clear – a slight trend seen in~~ As shown in Fig. 10, without the refinements, in the range $\mathrm{CBH} < 1\,\mathrm{km}$ 12 ASI-pairs with camera distance up to $1.6\,\mathrm{km}$ perform better than the ASI network in terms of RMSD and BIAS~~is overlaid by strong scattering. The variation of error metrics found between these systems may indicate further influences of the setup on accuracy apart from~~. As discussed in Sect. 4.2, in this range of reference CBH the ASI network could be improved by ASI-pairs with even smaller camera distance. The ~~lower frequency of observations of intermediate and large CBH is expected to cause a part of the observed scattering of the metrics between the various~~ applied refinements improve the accuracy notably. Figure 10 includes the error metrics received when simply averaging CBH measurements of all ASI-pairs. ~~Firstly, sporadic large errors may occur only in some of~~ The ASI network in both variants, with and without refinements, provides a significantly more accurate estimation of CBH in terms of RMSD and BIAS in most ranges of CBH compared to the simple approach.

The individual ASI-pairs and also the ASI-network exibit an RMSD of more than $180\,\mathrm{m}$ for all ranges of CBH. Based on this, we do not expect that the bin size of $100\,\mathrm{m}$ chosen for the distributions of conditional probability in Sect. 3.4 is a limiting factor to the accuracy of the ~~evaluated systems and dominate the received metrics for these. Secondly, from the statistics and from an inspection of the ASI images observations of higher CBH layers are likely to be found in the presence of a lower layer. As discussed in Sect. 3.1 the~~ ASI-based estimation of CBH in this study. Meanwhile, the underlying ASI-pairs ~~measure CBH of the most dominant cloud layer in the sense of optical thickness and area in the analyzed field of view of the sky. When for example, a CBH of $10\,\mathrm{km}$ is present the corresponding spatial area included has side lengths of $15.7\,\mathrm{km}$. For multi-cloud-layer conditions it is likely that within this window lower clouds are present which are recognized by an ASI-pair instead.More aggressive filtering of such multilayer situations included in the evaluation could reduce this influence but would further limit the database. The distance between the cameras used by an ASI-pair and the reference ceilometer are not found to have a significant influence on received accuracy in the evaluated data set. This was expected in part from the previously discussed effect that the~~ can nowcast 30 s-averages of solar irradiance at a spatial resolution of $5\,\mathrm{m} \times 5\,\mathrm{m}$. According to the considerations of Nouri et al. (2019b) and with the sun elevations occuring at the site, deviations in CBH may cause deviations in the positions of cloud shadow edges of at least $100\,\mathrm{m}$ under favorable conditions for the ASI-pairs ~~measure CBH of the most dominant cloud layer~~and also for the ASI-network. This deviation is much larger than the spatial resolution of these maps of solar irradiance. For certain applications, e.g. to control solar power plants (Nouri et al., 2020a), it may still be advantageous to provide maps of solar irradiance at a resolution finer than the uncertainty of cloud shadow edge positions, as the statistical properties of spatial variability may still be captured in these maps.

~~Based on these findings the ASI network combines the favorable properties of the involved~~

4.4.2 Influence of the camera distance on performance metrics

Lastly we discuss how camera distance influences the performance metrics of the ASI-pairs ~~. Over a single ASI-pair an improvement in accuracy is found as no ASI-pair can optimally cover the whole range of relevant CBH . With the achieved accuracy of the CBH measurement under all conditions at least a classification of the present cloud height is possible. CBH measurement by the ASI network is found to provide a small BIAS if $\mathrm{CBH} < 8\,\mathrm{km}$ is of interest. Therefore and given the~~

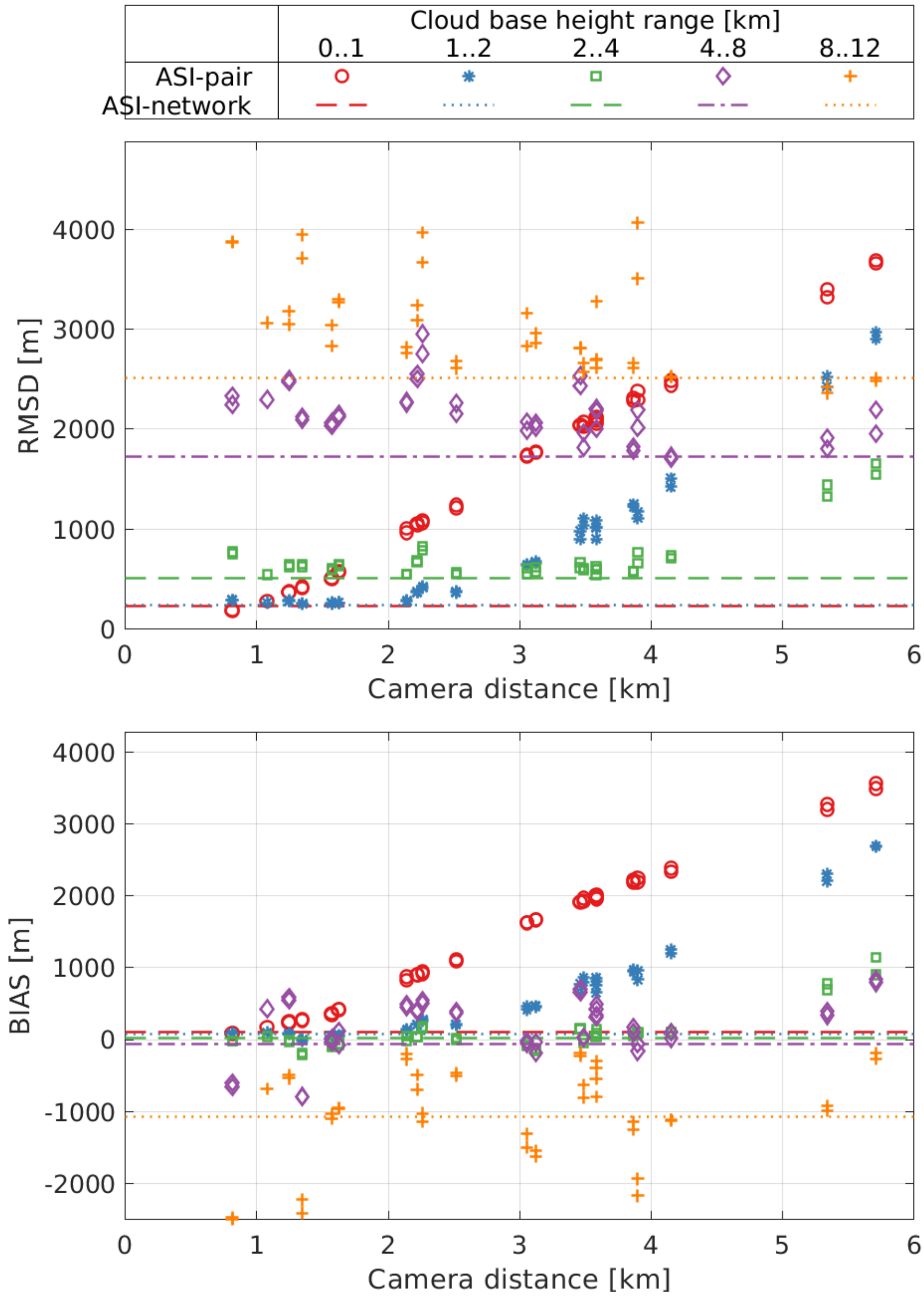

Figure 11. RMSD (top) and BIAS (bottom) received by 42 ASI-pairs utilizing camera distances in the range of 0.8…5.7 km and by the ASI network with refinements (no camera distance applicable) for the period 30 June 2019 to 27 September 2019.

~~different nature of both measurements, the accuracy of CBH~~ in different ranges of CBH and compare these results those of Kuhn et al. (2019) who studied the accuracy of ASI-pairs with camera distances in the range of 0.5...2.56 km. Figure 11 provides RMSD and BIAS received from the ASI network ~~is expected to improve further if an average CBH over a range of hours is of interest.~~

4.5 ~~Discussion of deviations in CBH measurement~~

~~For low CBH (CBH < 2 km) accuracy of the measurement by~~ and ASI-pairs ~~decreases with~~ and distinguishes the latter by camera distance. ~~This meets the expectation from Kuhn et al. (2019). Kuhn's study was limited to a maximum camera distance of 2.56 km. Additionally,~~ Metrics of the ASI network, with refinements, are given by horizontal lines. Kuhn et al. (2019) analyzed the accuracy of CBH measurement ~~was only analyzed~~ for three ranges of CBH defined by the limits $\{0, 3, 8, 12\}$ km. ~~We noticed that a finer classification of CBH as used~~ Overall, in the present study ~~yields more insights for small CBH. Figure 8 upper row provides the relative frequency of CBH readings from two exemplary ASI-pairs given a reference CBH. The camera distances of the ASI-pairs are 0.8 km (left) and 5.3 km (right) respectively. For reference CBH below a minimum value of around 2 km the ASI-pair with camera distance 5.3 km in most cases provides unreasonable readings scattering around 3.8 km. For ASI-pairs with smaller camera distance a similar behavior is observed while the respective minimum CBH reduces with reduced~~ the magnitudes of RMSD and BIAS range well below the values found by Kuhn et al. (2019).

For the CBH ranges 0...1 km and 1...2 km, Fig. 11 shows that BIAS is very small for ASI-pairs with small camera distance. ~~Accordingly, both RMSD and BIAS steadily increase~~ However, beginning at a camera distance of around 1.1 km and 2.5 km respectively, BIAS increases linearly with camera distance~~as shown in Fig. 11 for CBH~~ ~~$\in]0,1[$ km. Even for the~~. Consequently the same trend is visible for RMSD in these ranges of CBH. From the analysis in Sect. 4.2, this effect is clearly connected to the minimum CBH specific to an ASI-pair~~with camera distance 0.8 km a significant minimum CBH of 0.5 km is found (compare Fig. 8, left). In line with the discussion above for CBH~~ ~~$\in [1,2[$ km both metrics only increase from a camera distance of 2.5 km on~~'s camera distance. While the in study of Kuhn et al. (2019) the lowest CBH range covered 0...3 km, which reduces the influence of minimum CBH, a qualitatively similar relationship of camera distance and accuracy was found. ~~Minimum CBH of~~

For intermediate and large CBH (4...12 km) the ~~ASI-pair for this camera distance is identified to be 1.3 km~~correlation of camera distance and accuracy is less clear – a slight trend seen in RMSD and BIAS is overlaid by strong scattering. The variation of error metrics found between these systems may indicate further influences of the setup on accuracy apart from camera distance. On the other hand, the limited set of observations of high clouds may not be sufficiently representative to identify the influence of camera distance in the presence of other disturbances present in this benchmark, such as low clouds which may be present in spite of the applied filter.

~~For intermediate and large CBH (~~Overall, in the range of CBH > 4 km~~)~~, increased camera distance slightly improves the accuracy of CBH estimation. On average a reduction in RMSD of 500 m is suggested over the interval of studied camera distances. No significant influence is noticed for BIAS. From Kuhn et al. (2019) the influence of camera distance on accuracy was expected to be more significant in this range of CBH. ~~The influence of CBH on accuracy of the measurement coincides~~

~~qualitatively between both studies. In both cases a positive BIAS is attested for small CBH and negative BIAS for large CBH. RMSD is found to increase with CBH in absolute values. However, in the present study the magnitudes of RMSD and BIAS range well below the values found in Kuhn et al. (2019).~~

~~Beside camera distance the~~ Further, the orientation of the ~~camera~~ ASI-pair's axis to the present direction of cloud movement was considered as an influence on accuracy in Kuhn et al. (2019). ~~Based on that study~~ ASI-pairs may measure CBH more accurately if ~~their camera~~ the ASI-pair's axis is aligned with the direction of cloud motion. ~~To study this effect the~~ The direction of cloud motion was retrieved from ASI UOL as ~~discussed~~ described in Sect. 3.2 ~~. Then~~ and the dataset was ~~restricted to times in which clouds moved~~ filtered to timestamps with cloud motion from west to east. Accuracies of ASI-pairs with similar camera distance but different orientation of the ~~camera axis over the direction of cloud motion~~ ASI-pair's axis were compared. In this comparison no correlation of ~~camera alignment over the direction of cloud motion and accuracy was recognized.~~ accuracy and the alignment of the ASI-pair's axis over the direction of cloud motion was recognized.

~~The behavior seen for CBH below a minimum value can be understood as follows. For small CBH and large camera distance the overlapping area (i.e. the fraction of the sky captured by both cameras) becomes small and corresponds to clouds located between both ASIs (Nguyen and Kleissl, 2014). These clouds are observed from very different perspectives by both ASIs. The difference in perspective may be expressed by the angular distance between a cloud's depiction in both ASIs' views. In hemispherical ASI images the similarity of a specific cloud observed by both ASIs reduces with this angular distance. Likewise, the representation of two clouds, that are randomly selected from the paired ASIs' sky images respectively, will appear more similar if they are observed at a small angular distance to each other. Therefore, erroneously matched cloud edges will typically be separated by a moderate angular distance. Thus, the likelihood to match cloud objects correctly which are observed at a large angular distance by the paired ASIs is small. If actual CBH relative to camera distance is small the fraction of invalid readings (indicating not any match) increases and concurrently a large share of the valid readings goes back to mismatches. Estimated cloud height scales inversely with angular distance of matched cloud patterns for stereoscopic approaches to measure CBH. Consequently, the negative bias of angular distance in the matching translates into a positive bias of estimated CBH. Except for this distinct effect the error metrics of all studied ASI-pairs are very similar for~~ ~~$\mathrm{CBH} < 4\,\mathrm{km}$.~~

Based on these findings we recommend to chose camera distance of a single ASI-pair, that is not part of an ASI network, based on the smallest CBH (CBH_{min}) which is of interest at a site. This consideration differs from previous studies by Nguyen and Kleissl (2014) and Kuhn et al. (2019) which suggest, based on theoretical and experimental findings respectively, to optimize camera distance for the most frequent or most relevant CBH. Our experimental results suggest that camera distance of a single ASI-pair should if possible not be chosen larger than ~~$1.4\,\mathrm{CBH}_{min}$~~ $1.4 \times \mathrm{CBH}_{min}$ and in no case larger than $3 \times \mathrm{CBH}_{min}$. For the meteorological conditions studied here, ASI-pairs with even smaller camera distances than $0.8\,\mathrm{km}$ would be beneficial to cover the range $\mathrm{CBH} < 0.5\,\mathrm{km}$.

~~Figure 10 provides error metrics for the ASI network both with and without refinements described in Sect. 3.3. Without the refinements, in the range~~ ~~$\mathrm{CBH} < 1\,\mathrm{km}$~~ ~~12 ASI-pairs with camera distance up to~~ ~~$1.6\,\mathrm{km}$~~ ~~perform better than the ASI network in terms of RMSD and BIAS. In this range of CBH the ASI network suffers strongly from overestimation of CBH related to the found minimum CBH of involved ASI-pairs. For sites like Oldenburg at which low cloud conditions are dominant (see Sect.~~

~~3.2) the presented approach without refinements would require a larger share of ASI-pairs with small camera distances of even less than 0.8 km. However, the refinements succeed to improve these shortcomings. Figure 10 also includes the error metrics received when simply averaging CBH measurements of all ASI-pairs. The ASI network in both variants, with and without refinements, provides a significantly more accurate estimation of CBH in terms of RMSD and BIAS in most ranges of CBH compared to the simple approach.~~

5 Conclusions

In this study, a method was presented and benchmarked to estimate cloud base height (CBH) by a network of all-sky-imagers (ASIs). The ASI network-based estimation of CBH aims to combine the measurements of CBH from ASI-pairs arranged in proximity and organized in a network. Conditional probabilities are modeled from historic CBH measurements received from ASI-pairs and a reference ceilometer. These indicate the probability that an ASI-pair with specific camera distance would deliver a specific CBH reading if true CBH actually was in a specific range. In the inference the ASI network uses this knowledge to calculate the likeliest CBH given the readings of CBH from individual ASI-pairs. Additionally, accuracy of CBH measured by 42 independent all-sky-imager (ASI)-pairs over a period of 90 days was analyzed. This validation extended prior studies of the analyzed system to the conditions of a Central-European climate (Cfb) and to an unprecedented variety of camera alignments and camera distances ($0.8...5.7$ km).

The influence of camera distance on the accuracy of ASI-based estimation of CBH was less pronounced than suggested by prior studies. For low clouds ($\mathrm{CBH} < 4$ km) small camera distances were found to lead to most accurate measurements. Under these conditions deviations were found to increase steadily with camera distance as described in the literature. For higher clouds (especially for $\mathrm{CBH} > 8$ km) larger camera distances were found to affect received accuracy positively. However, this effect was small compared to the expectation. As main cause of deviations a minimum CBH was identified which is specific to each ASI-pair. Minimum CBH was found to increase steadily with camera distance of an ASI-pair. Below this minimum CBH ASI-pairs were found to return non-physical and positively biased readings.

When selecting a camera distance for an ASI-pair with stereoscopic estimation of CBH based on cross-correlation, this study suggests to consider the following depending on the meteorological conditions on-site. ASI-pairs with camera distance < 2 km are accurate only for CBH up to 4 km. ASI-pairs with camera distance > 3 km are slightly more accurate than ASI-pairs with smaller camera distance for $\mathrm{CBH} \geq 4$ km, but much less accurate for $\mathrm{CBH} < 4$ km than ASI-pairs with smaller camera distance. For ASI-pairs which are set up at sites with a similar distribution of CBH as in our study, we recommend including camera distances smaller than 1.8 km. If mostly medium-height or high clouds are expected a greater camera distance is preferable. If possible multiple setups also including ASI-pairs with small (< 0.8 km) and larger camera distances (> 1.8 km) are recommended to increase accuracy for all CBH ranges. However, larger camera distances can help to increase the spatial coverage of an ASI network with a given number of cameras, which is also of advantage. A trade-off between CBH accuracy and coverage or costs must hence be found for ASI networks.

The presented approach to merge measurements of ASI-pairs in an ASI network combined favored properties of the individual ASI-pairs. For all five ranges, that were defined for reference CBH readings by the bin edges $0,1,2,4,8,12$ km, the ASI network provides a measurement that is among the most accurate ones compared to individual ASI-pairs in terms of RMSD. Individual ASI-pairs slightly outperformed the network but only for single intervals of CBH. In terms of BIAS the same finding was received except for the range of $\mathrm{CBH} \in [8,12]$ km. In this CBH range the ASI network yields an average BIAS, compared to the ASI-pairs, as all of the ASI-pairs are biased for these conditions.

The presented ASI network-based approach to CBH-measurement can be transferred to other sites using the conditional probabilities of CBH found at the Oldenburg site. Found distributions may then be extended to include more frequent observations of high clouds. Especially regarding its geometric dimensions and spatial coverage the used setup is suited for airports and large or networked solar power systems.

Based on the present study, the proposed approach to measure CBH in an ASI network will in future be enhanced by first extending the utilized statistics of measured CBH with data from other sites at which a combination of ASI-pair and ceilometer is available. Such an extended dataset will additionally allow to use more elaborate statistical methods including neural networks. A procedure to generate irradiance nowcasts based on the whole ASI network utilizing the method to estimate CBH described here is under development.

Data availability. Used all-sky-images and ceilometer measurements are property of DLR, Institut für Vernetzte Energiesysteme and can be requested from the corresponding author. Processed data presented in this publication is available on request from the corresponding author (niklas.blum@dlr.de).

Appendix A: Details on the retrieval of conditional probabilities

A1 Retrieval of raw joint frequency distributions

CBH from the respective ASI-pair and from the ceilometer are processed by a moving-median filter with a window of 10 min. The joint frequency distribution of CBH measured by ceilometer h_{Ref} and the respective ASI-pair h_{ASI} is computed from these simultaneously acquired time series. That means, the frequency is calculated with which (h_{Ref}, h_{ASI}) is observed in a discrete grid cell defined by the interval $[j\Delta h, (j+1)\Delta h[$ for h_{Ref} and the interval $[k\Delta h, (k+1)\Delta h[$ for h_{ASI}, where $j,k \in \{0,1,2,...,N-1\}$, where N is the number of bins used for CBH in the analysis. A bin size $\Delta h = 100$ m is chosen in a trade-off between sources of error. Finer bins will allow to represent the distributions at higher resolution and will thus allow for higher resolved measurements of CBH in the network. However, the size of the used data set is limited which makes it difficult to model these distributions at highest resolution. The bin size chosen here is expected to limit the achievable uncertainty of the measurement to a minimum level of 100 m. Joint frequency distributions modeled here are restricted to a maximum CBH of 12 km. This yields $N = 120$.

A2 Filtering operations applied

First, a weighted mean filter is applied between original joint frequency distributions F_l received from all ASI-pairs with camera distance d, this yields $F_{l,filter\ 1}$:

$$F_{l,filter\ 1} = \frac{\sum_m w_{l,m} F_m}{\sum_m w_{l,m}}. \tag{A1}$$

For the joint frequency distribution F_l of each respective ASI-pair l, weights $w_{l,m}$ are used that include ASI-pairs with similar camera distance. More precisely, a triangular window, based on the difference of camera distance $\Delta d_{l,m}$ of ASI-pair m compared to ASI-pair l, is used that is defined by

$$w_{l,m} = max(0, 1 - \Delta d_{l,m}/0.5\ \mathrm{km}). \tag{A2}$$

We decompose each distribution $F_{l,filter\ 1}$ by conditional filters into three separate *modes*. In the second step, we apply to each mode a Gaussian filter g_σ with distinct standard deviation σ_{mode} of the Gaussian kernel. The subscript *mode* indicates the specific mode for which σ_{mode} is applied. The first mode is constituted by all outlier observations. Outliers are defined here as grid cells (h_{Ref}, h_{ASI}) for which ASI-pair measurement of CBH h_{ASI} deviates by more than 1.5 km from the ceilometer reading h_{Ref}:

$$F_{l,outlier}(h_{Ref}, h_{ASI}) = \begin{cases} F_{l,filter\ 1}(h_{Ref}, h_{ASI}), & |h_{ASI} - h_{Ref}| > 1.5\ \mathrm{km} \\ 0, & \text{else.} \end{cases} \tag{A3}$$

Such outliers will contain a large random component. We expect that in a reproduction of the experiment, a similar number of outliers will be received, while the joint frequency found for a single grid cell (h_{Ref}, h_{ASI}) may vary significantly. Therefore, the strongest filter is applied to this mode using $\sigma_{outlier} = 1$ km.

The second mode is constituted by grid cells that are not part of the first mode and feature a joint frequency less than the average over all grid cells of the joint frequency distribution:

$$F_{l,inconfident}(h_{Ref}, h_{ASI}) = \begin{cases} F_{l,filter\ 1}(h_{Ref}, h_{ASI}), & |h_{ASI} - h_{Ref}| \leq 1.5\ \mathrm{km} \\ & \wedge\ F_{l,filter\ 1}(h_{Ref}, h_{ASI}) < \mathrm{mean}(F_{l,filter\ 1}) \\ 0, & \text{else.} \end{cases} \tag{A4}$$

The comparably small number of observations in these grid cells is expected to cause an increased uncertainty of the estimated joint frequencies. For this mode, $\sigma_{inconfident} = 0.5$ km is applied.

The third mode $F_{l,confident}(h_{Ref}, h_{ASI})$ makes up the complementary of the first and second mode. It contains grid cells that are observed with an at least average joint frequency and which are not classified as outliers:

$$F_{l,confident}(h_{Ref}, h_{ASI}) = \begin{cases} F_{l,filter\ 1}(h_{Ref}, h_{ASI}), & |h_{ASI} - h_{Ref}| \leq 1.5\ \mathrm{km} \\ & \wedge\ F_{l,filter\ 1}(h_{Ref}, h_{ASI}) \geq \mathrm{mean}(F_{l,filter\ 1}) \\ 0, & \text{else.} \end{cases} \tag{A5}$$

Joint frequencies in these grid cells are considered to have a comparably high accuracy. To avoid a loss of precision and ultimately a loss of accuracy in the estimation of CBH, a small value of $\sigma_{confident} = 0.1$ km is used. The three filtered modes g_σ are summed to receive the smoothened joint frequency distribution

$$F_{l,filter\ 2} = g_{\sigma_{outlier}}(F_{l,outlier}) + g_{\sigma_{inconfident}}(F_{l,inconfident}) + g_{\sigma_{confident}}(F_{l,confident}). \tag{A6}$$

For all grid cells, joint frequency is increased to a minimum value of 0.5 to avoid underestimations of joint frequency. This value is chosen to be half of the joint frequency associated with a single actual observation in a grid-cell.

Each joint frequency distribution is normalized with the sum of all joint frequency grid cells. In this way, a probability mass function $P(h_{Ref}, h_{ASI})$ (also known as discrete density function) to measure a certain CBH with the respective ASI-pair and to coincidentally measure a certain CBH with the ceilometer is yielded. The conditional probability $P(h_{ASI} \mid h_{Ref})$ to receive a certain CBH reading from an ASI-pair, given that the ceilometer measures some certain CBH, is calculated by dividing the respective probability mass function by the marginal distribution of CBH measured by the ceilometer. The latter distribution gives the probability to receive CBH from the ceilometer within a certain bin h_{Ref} regardless of which CBH reading is simultaneously received from an ASI-pair. The distribution can be derived from any of the probability mass functions by summing all grid cells of the probability mass function which correspond to the respective bin h_{Ref} of CBH measured by the ceilometer.

A3 Representation of intervals of camera distance

The inference procedure represents each range i of camera distance bounded by the limits $\{0.5, 1, 1.5, ..., 6\}$ km by a single distribution of conditional probability. For each range of camera distance, the distribution of conditional probability, which corresponds to the camera distance closest to the center of this range, is selected. For example, for the range $i = 2$ representing camera distances $1 ... 1.5$ km, the center of the range would be 1.25 km. For the camera distances 1.081, 1.247 and 1.352 km, conditional probabilities have been modeled. Consequently, for this range of camera distance, the distribution of conditional probability corresponding to the camera distance 1.247 km is used.

Appendix B: Comparison of CBH time series

B1 Estimation of CBH during a clear sky period

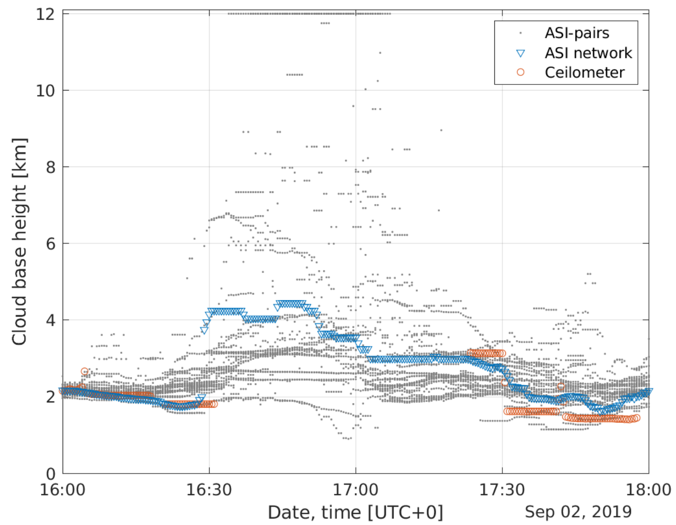

Figure B1. Detail view of CBH measured by ASI-pairs (grey dots), by the ASI network (blue triangles) and ceilometer (red circles) during a period with low sky coverage. Around 17:00 approaching clouds are viewed close to the horizon by all ASIs.

Figure B1 provides a detail view of CBH measured by ASI-pairs, by the ASI network and by the ceilometer during a mostly clear period on 02 September 2019. The period is discussed in Sect. 4.1.

B2 Comparison of CBH measurements for another exemplary day

Figure B2 shows CBH on 06 August 2019 again measured by ceilometer, by all available ASI-pairs and by the ASI network. This day, similar to 02 September 2019, discussed previously, includes multi-layer conditions with high layers overlaid by low layers, resulting in similar observations. In the morning and evening high cloud layers are dominant. The CBH of these varies in the range of 7...11 km according to the ceilometer. The range of CBH from ASI-pairs reflects this spread. Still, it is not obvious which of the ASI-pair based observations would be the most appropriate. From the ASI network a rather steady CBH estimation results which most of the time reflects the dominant CBH layer as recognized by the ceilometer. The combined estimation misses physically meaningful variations of CBH typically towards higher values recognized by the ceilometer. Also for this day time series of CBH and corresponding ASI images were compared. Again large underestimations of CBH by the ASI network (at 05:30, 08:15, 10:00, 12:30, 16:00) were traced back to the ASI-based estimations responding stronger to lower optically denser low cloud layers which pass the vicinity of the urban area (compare Fig. B3).

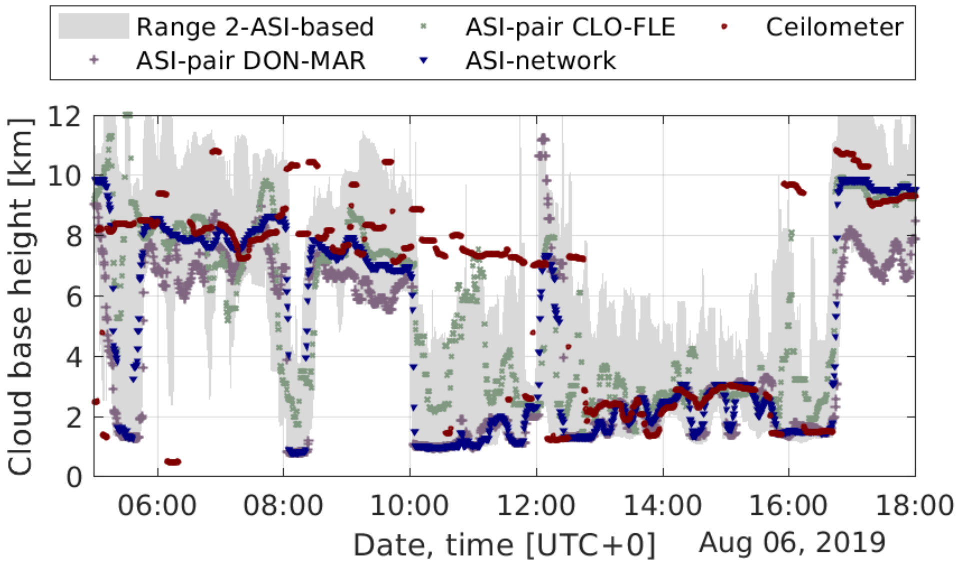

Figure B2. Time series of cloud base height for an exemplary day (06 August 2019) measured by 42 ASI-pairs (grey filled), by two exemplary ASI-pairs DON-MAR and CLO-FLE with respective camera distances 0.8 and 4.2 km, by the ASI network with refinements and by a ceilometer in the urban area of Oldenburg.

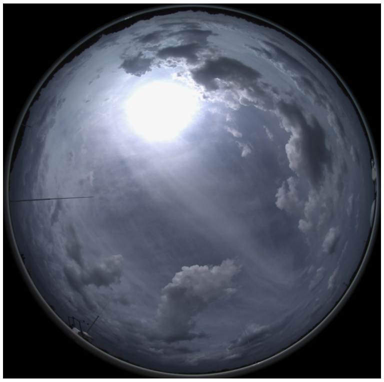

Figure B3. Sky image taken by ASI UOL representing a multi-cloudlayer situation on 06 August 2019 12:35

Author contributions. Investigation and conceptualization was carried out by NB. NB with contributions by BN, SW developed the methodology and software. TS, OL, JS provided used experimental resources and data curation. NB prepared the original draft and created visualizations. All authors contributed to writing, editing and review of the publication. SW, DH, AK, RPP supervised the presented work.

Competing interests. The authors declare that they have no conflict of interest.

Acknowledgements. This research received funding from the European Union's Horizon 2020 research and innovation programme under grant agreement No 864337 (Smart4RES project). We would like to thank Norman Noske for his support in the setup and maintenance of the Eye2Sky ASI network.

References

Aides, A., Levis, A., Holodovsky, V., Schechner, Y. Y., Althausen, D., and Vainiger, A.: Distributed Sky Imaging Radiometry and Tomography, in: IEEE Xplore/ 2020 IEEE International Conference on Computational Photography (ICCP), pp. 1–12, Saint Louis, MO, USA, 24-26 April 2020, 2020.

Allmen, M. C. and Kegelmeyer Jr, W. P.: The Computation of Cloud-Base Height from Paired Whole-Sky Imaging Cameras, Journal of Atmospheric Oceanic Technology, 13, 97–113, https://doi.org/10.1175/1520-0426(1996)013<0097:TCOCBH>2.0.CO;2, 1996.

Beekmans, C., Schneider, J., Läbe, T., Lennefer, M., Stachniss, C., and Simmer, C.: Cloud photogrammetry with dense stereo for fisheye cameras, Atmospheric chemistry and physics, 16, 231–14, https://doi.org/10.5194/acp-16-14231-2016, 2016.

Bieliński, T.: A parallax shift effect correction based on cloud height for geostationary satellites and radar observations, Remote Sensing, 12, 365, https://doi.org/10.3390/rs12030365, 2020.

Blanc, P., Massip, P., Kazantzidis, A., Tzoumanikas, P., Kuhn, P., Wilbert, S., Schüler, D., and Prahl, C.: Short-term forecasting of high resolution local DNI maps with multiple fish-eye cameras in stereoscopic mode, AIP conference Proceedings, 1850, 140 004, https://doi.org/10.1063/1.4984512, 2017.

Blum, N., Schmidt, T., Nouri, B., Wilbert, S., Heinemann, D., Schmidt, T., Kuhn, P., Zarzalejo, L. F., and Pitz-Paal, R.: Optimierte Gruppierung verschiedener Wolkenkameras im Oldenburger Nowcasting Netzwerk, in: Tagungsunterlagen/ 34. PV-Symposium Bad Staffelstein, pp. 552–562, Bad Staffelstein, Germany, 19-21 March 2019, 2019a.

Blum, N., Schmidt, T., Nouri, B., Wilbert, S., Peerlings, E., Heinemann, D., Schmidt, T., Kuhn, P., Kazantzidis, A., Zarzalejo, L. F., and Pitz-Paal, R.: Nowcasting of Irradiance Using a Network of All-Sky-Imagers, in: EU PVSEC 2019 Proceedings/ 36th European Photovoltaic Solar Energy Conference and Exhibition, pp. 1403 – 1409, Marseille, France, 09-13 September 2019, https://doi.org/10.4229/EUPVSEC20192019-5DO.2.1, https://www.eupvsec-proceedings.com/proceedings?fulltext=Nowcasting&paper=48484, 2019b.

Chan, K. L., Wiegner, M., Flentje, H., Mattis, I., Wagner, F., Gasteiger, J., and Geiß, A.: Evaluation of ECMWF-IFS (version 41R1) operational model forecasts of aerosol transport by using ceilometer network measurements, Geoscientific Model Development, 11, 3807–3831, https://doi.org/10.5194/gmd-11-3807-2018, 2018.

Cirés, E., Marcos, J., de la Parra, I., García, M., and Marroyo, L.: The potential of forecasting in reducing the LCOE in PV plants under ramp-rate restrictions, Energy, 188, 116 053, https://doi.org/10.1016/j.energy.2019.116053, 2019.

Costa-Surós, M., Calbó, J., González, J., and Martin-Vide, J.: Behavior of cloud base height from ceilometer measurements, Atmospheric research, 127, 64–76, https://doi.org/10.1016/j.atmosres.2013.02.005, 2013.

de Haij, M., Apituley, A., Koetse, W., and Bloemink, H.: Transition towards a new ceilometer network in the Netherlands: challenges and experiences, in: Instruments and Observing Methods Report No. 125/ WMO Technical Conference on Meteorological and Environmental Instruments and Methods of Observation (CIMO TECO 2016), Madrid, Spain, 27-30 September 2016, https://library.wmo.int/index.php?lvl=notice_display&id=19676#.XirnGzJKiUk, 2016.

Fabel, Y., Nouri, B., Wilbert, S., Blum, N., Triebel, R., Hasenbalg, M., Kuhn, P., Zarzalejo, L. F., and Pitz-Paal, R.: Applying self-supervised learning for semantic cloud segmentation of all-sky images, Atmospheric Measurement Techniques Discussions, 2021, 1–20, https://doi.org/10.5194/amt-2021-1, 2021.

Ghosh, S., Rahman, S., and Pipattanasomporn, M.: Distribution voltage regulation through active power curtailment with PV inverters and solar generation forecasts, IEEE Transactions on Sustainable Energy, 8, 13–22, https://doi.org/10.1109/TSTE.2016.2577559, 2016.

Görsdorf, U., Mattis, I., Pittke, G., Bravo-Aranda, J. A., Brettle, M., Cermak, J., Drouin, M.-A., Geiß, A., Haefele, A., and Hervo, M.: The ceilometer inter-comparison campaign CeiLinEx2015 — Cloud detection and cloud base height, in: Instruments and Observing Methods Report No. 125/ WMO Technical Conference on Meteorological and Environmental Instruments and Methods of Observation (CIMO TECO 2016), pp. 27–30, Madrid, Spain, 27-30 September 2016, https://library.wmo.int/index.php?lvl=notice_display&id=19676#.XirnGzJKiUk, 2016.

Hamann, U., Walther, A., Baum, B., Bennartz, R., Bugliaro, L., Derrien, M., Francis, P. N., Heidinger, A., Joro, S., Kniffka, A., Le Gléau, H., Lockhoff, M., Lutz, H. J., Meirink, J. F., Minnis, P., Palikonda, R., Roebeling, R., Thoss, A., Platnick, S., Watts, P., and Wind, G.: Remote sensing of cloud top pressure/height from SEVIRI: analysis of ten current retrieval algorithms, Atmospheric Measurement Techniques, 7, 2839–2867, https://doi.org/10.5194/amt-7-2839-2014, 2014.

Heese, B., Flentje, H., Althausen, D., Ansmann, A., and Frey, S.: Ceilometer lidar comparison: backscatter coefficient retrieval and signal-to-noise ratio determination, Atmospheric Measurement Techniques, 3, 1763–1770, https://doi.org/10.5194/amt-3-1763-2010, 2010.

Hogan, R. J., O'Connor, E. J., and Illingworth, A. J.: Verification of cloud-fraction forecasts, Quarterly Journal of the Royal Meteorological Society: A journal of the atmospheric sciences, applied meteorology physical oceanography, 135, 1494–1511, https://doi.org/10.1002/qj.481, 2009.

Howie, R. M., Paxman, J., Bland, P. A., Towner, M. C., Cupak, M., Sansom, E. K., and Devillepoix, H. A.: How to build a continental scale fireball camera network, Experimental Astronomy, 43, 237–266, https://doi.org/10.1007/s10686-017-9532-7, 2017.

Isaac, G. A., Bailey, M., Boudala, F. S., Burrows, W. R., Cober, S. G., Crawford, R. W., Donaldson, N., Gultepe, I., Hansen, B., Heckman, I., Huang, L. X., Ling, A., Mailhot, J., Milbrandt, J. A., Reid, J., and Fournier, M.: The Canadian Airport Nowcasting System (CAN-Now), Meteorological Applications, 21, 30–49, https://doi.org/10.1002/met.1342, 2014.

Kaur, A., Nonnenmacher, L., Pedro, H. T., and Coimbra, C. F.: Benefits of solar forecasting for energy imbalance markets, Renewable Energy, 86, 819–830, https://doi.org/10.1016/j.renene.2015.09.011, 2016.

Khlopenkov, K., Spangenberg, D., and Smith Jr, W. L.: Fusion of Surface Ceilometer Data and Satellite Cloud Retrievals in 2D Mesh Interpolating Model with Clustering, in: Proc. SPIE 11152, Remote Sensing of Clouds and the Atmosphere XXIV/ SPIE Remote Sensing 2019, p. 111521F, Strasbourg, France, 9 October 2019, https://doi.org/10.1117/12.2533370, 2019.

Kottek, M., Grieser, J., Beck, C., Rudolf, B., and Rubel, F.: World map of the Köppen-Geiger climate classification updated, Meteorologische Zeitschrift, 15, 259–263, https://doi.org/10.1127/0941-2948/2006/0130, 2006.

Kuhn, P., Nouri, B., Wilbert, S., Prahl, C., Kozonek, N., Schmidt, T., Yasser, Z., Ramirez, L., Zarzalejo, L., and Meyer, A.: Validation of an all-sky imager–based nowcasting system for industrial PV plants, Progress in Photovoltaics: Research and Applications, 26, 608–621, https://doi.org/10.1002/pip.2968, 2018a.

Kuhn, P., Wirtz, M., Killius, N., Wilbert, S., Bosch, J. L., Hanrieder, N., Nouri, B., Kleissl, J., Ramirez, L., Schroedter-Homscheidt, M., Heinemann, D., Kazantzidis, A., Blanc, P., and Pitz-Paal, R.: Benchmarking three low-cost, low-maintenance cloud height measurement systems and ECMWF cloud heights against a ceilometer, Solar Energy, 168, 140–152, https://doi.org/10.1016/j.solener.2018.02.050, 2018b.

Kuhn, P., Nouri, B., Wilbert, S., Hanrieder, N., Prahl, C., Ramirez, L., Zarzalejo, L., Schmidt, T., Yasser, Z., Heinemann, D., Tzoumanikas, P., Kazantzidis, A., Kleissl, J., Blanc, P., and Pitz-Paal, R.: Determination of the optimal camera distance for cloud height measurements with two all-sky imagers, Solar Energy, 179, 74–88, https://doi.org/10.1016/j.solener.2018.12.038, 2019.

Law, E. W., Prasad, A. A., Kay, M., and Taylor, R. A.: Direct normal irradiance forecasting and its application to concentrated solar thermal output forecasting–A review, Solar Energy, 108, 287–307, https://doi.org/10.1016/j.solener.2014.07.008, 2014.

Lufft: Manual Cloud Height Sensor CHM 15k, Manual 8350.mep, G. Lufft Mess- und Regeltechnik GmbH, Fellbach, Germany, 2018.

Luhmann, T.: Nahbereichsphotogrammetrie: Grundlagen, Methoden und Anwendungen, Wichmann Verlag, Heidelberg, Germany, 2000.

Macke, A., Seifert, P., Baars, H., Barthlott, C., Beekmans, C., Behrendt, A., Bohn, B., Brueck, M., Bühl, J., and Crewell, S.: The HD (CP) 2 observational prototype experiment (HOPE)-An overview, Atmospheric chemistry and physics, 17, 4887–4914, https://doi.org/10.5194/acp-17-4887-2017, 2017.

Martucci, G., Milroy, C., and ODowd, C. D.: Detection of cloud-base height using Jenoptik CHM15K and Vaisala CL31 ceilometers, Journal of Atmospheric Oceanic Technology, 27, 305–318, https://doi.org/10.1175/2009JTECHA1326.1, 2010.

Mejia, F. A., Kurtz, B., Levis, A., de la Parra, Í., and Kleissl, J.: Cloud tomography applied to sky images: A virtual testbed, Solar Energy, 176, 287–300, https://doi.org/10.1016/j.solener.2018.10.023, 2018.

Mobotix: Technical Specifications MOBOTIX Q25 Hemispheric, Data sheet, Mobotix AG, Langmeil, Germany, https://www.mobotix.com/sites/default/files/2017-10/Mx_TS_Q25_en_20170515.pdf, 2017.

Nguyen, D. and Kleissl, J.: Stereographic methods for cloud base height determination using two sky imagers, Solar Energy, 107, 495–509, https://doi.org/10.1016/j.solener.2014.05.005, 2014.

Noh, Y.-J., Forsythe, J. M., Miller, S. D., Seaman, C. J., Li, Y., Heidinger, A. K., Lindsey, D. T., Rogers, M. A., and Partain, P. T.: Cloud-Base Height Estimation from VIIRS. Part II: A Statistical Algorithm Based on A-Train Satellite Data, Journal of Atmospheric and Oceanic Technology, 34, 585–598, https://doi.org/10.1175/JTECH-D-16-0110.1, 2017.

Nouri, B., Kuhn, P., Wilbert, S., Prahl, C., Pitz-Paal, R., Blanc, P., Schmidt, T., Yasser, Z., Santigosa, L. R., and Heineman, D.: Nowcasting of DNI maps for the solar field based on voxel carving and individual 3D cloud objects from all sky images, AIP Conference Proceedings, 2033, 190 011, https://doi.org/10.1063/1.5067196, 2018.

Nouri, B., Kuhn, P., Wilbert, S., Hanrieder, N., Prahl, C., Zarzalejo, L., Kazantzidis, A., Blanc, P., and Pitz-Paal, R.: Cloud height and tracking accuracy of three all sky imager systems for individual clouds, Solar Energy, 177, 213–228, https://doi.org/10.1016/j.solener.2018.10.079, 2019a.

Nouri, B., Wilbert, S., Kuhn, P., Hanrieder, N., Schroedter-Homscheidt, M., Kazantzidis, A., Zarzalejo, L., Blanc, P., Kumar, S., and Goswami, N.: Real-Time Uncertainty Specification of All Sky Imager Derived Irradiance Nowcasts, Remote Sensing, 11, 1059, https://doi.org/10.3390/rs11091059, 2019b.

Nouri, B., Wilbert, S., Segura, L., Kuhn, P., Hanrieder, N., Kazantzidis, A., Schmidt, T., Zarzalejo, L., Blanc, P., and Pitz-Paal, R.: Determination of cloud transmittance for all sky imager based solar nowcasting, Solar Energy, 181, 251–263, https://doi.org/10.1016/j.solener.2019.02.004, 2019c.

Nouri, B., Noureldin, K., Schlichting, T., Wilbert, S., Hirsch, T., Schroedter-Homscheidt, M., Kuhn, P., Kazantzidis, A., Zarzalejo, L. F., Blanc, P., Yasser, Z., Fernández, J., and Pitz-Paal, R.: Optimization of parabolic trough power plant operations in variable irradiance conditions using all sky imagers, Solar Energy, 198, 434–453, https://doi.org/10.1016/j.solener.2020.01.045, 2020a.

Nouri, B., Wilbert, S., Blum, N., Kuhn, P., Schmidt, T., Yasser, Z., Schmidt, T., Zarzalejo, L. F., Lopes, F. M., Silva, H. G., Schroedter-Homscheidt, M., Kazantzidis, A., Raeder, C., Blanc, P., and Pitz-Paal, R.: Evaluation of an All Sky Imager Based Nowcasting System for Distinct Conditions and Five sites, AIP Conference Proceedings, 2303, 180 006, https://doi.org/10.1063/5.0028670, 2020b.

Peng, Z., Yu, D., Huang, D., Heiser, J., Yoo, S., and Kalb, P.: 3D cloud detection and tracking system for solar forecast using multiple sky imagers, Solar Energy, 118, 496–519, https://doi.org/10.1016/j.solener.2015.05.037, 2015.

Reynolds, D. W., Clark, D. A., Wilson, F. W., and Cook, L.: Forecast-Based Decision Support for San Francisco International Airport: A NextGen Prototype System That Improves Operations during Summer Stratus Season, Bulletin of the American Meteorological Society, 93, 1503–1518, https://doi.org/10.1175/BAMS-D-11-00038.1, 2012.

Savoy, F. M., Lemaitre, J. C., Dev, S., Lee, Y. H., and Winkler, S.: Cloud base height estimation using high-resolution whole sky imagers, in: 2015 IEEE International Geoscience and Remote Sensing Symposium (IGARSS), pp. 1622–1625, Milan, Italy, 26-31 July 2015, 2016.

Scaramuzza, D., Martinelli, A., and Siegwart, R.: A Toolbox for Easily Calibrating Omnidirectional Cameras, in: 2006 IEEE/ RSJ International Conference on Intelligent Robots and Systems, pp. 5695–5701, Beijing, China, 9-15 October 2006, https://doi.org/10.1109/IROS.2006.282372, 2006.

Schmidt, T., Kalisch, J., Lorenz, E., and Heinemann, D.: Evaluating the spatio-temporal performance of sky-imager-based solar irradiance analysis and forecasts, Atmospheric Chemistry and Physics, 16, 3399–3412, https://doi.org/10.5194/acp-16-3399-2016, 2016.

Schmidt, T., Heinemann, D., Vogt, T., Blum, N., Nouri, B., Wilbert, S., and Kuhn, P.: Energiemeteorologisches Wolkenkameranetzwerk für die hochaufgelöste Kurzfristprognose der solaren Einstrahlung, in: DACH-Tagung, Garmisch-Partenkirchen, Deutschland, 18-22 March 2019, 2019.

Sky cameras: https://www.solar-repository.sg/sky-cameras, last accessed: 8 July 2020, 2020.

Wang, G., Kurtz, B., and Kleissl, J.: Cloud base height from sky imager and cloud speed sensor, Solar Energy, 131, 208–221, https://doi.org/10.1016/j.solener.2016.02.027, 2016.

Wessel, B., Huber, M., Wohlfart, C., Marschalk, U., Kosmann, D., and Roth, A.: Accuracy assessment of the global TanDEM-X Digital Elevation Model with GPS data, ISPRS Journal of Photogrammetry and Remote Sensing, 139, 171–182, https://doi.org/10.1016/j.isprsjprs.2018.02.017, 2018.

World Meteorological Organization, W.: Guide to meteorological instruments and methods of observation, vol. I –Measurement of Meteorological Variables of *WMO- No. 8*, WMO, Geneva, Switzerland, 29 edn., 2018.